5

Quantifying the River Aquifer Exchanges in Varuna River Basin Amid Climate Change

5.1 INTRODUCTION

Small rivers constitute the foundational framework of an extensive river basin. Originating from first-order channels, these small GW-fed tributaries significantly enhance the hydrological regime of larger rivers. Additionally, they foster the development of distinct riparian zones and ecologies, thereby playing a crucial role in the biodiversity and ecological health of the river basin.

Exchanges between rivers and aquifers play a critical role in the sustainability of small, GW-fed rivers. These interactions are essential for sustaining water availability, as they maintain both GW levels and streamflow, particularly during periods of low flow (C. Konrad, 2006; Wöhling et al., 2018). This connectivity ensures a continuous water supply to the river, which is essential for sustaining ecosystems during dry periods (Ronayne et al., 2017). The processes of exchange demonstrate a high degree of dynamism and exhibit significant variability in response to hydrological conditions, including precipitation events and levels of river discharge (Bartsch et al., 2014; Unland et al., 2015). The hyporheic zone, where river water and GW mi, is a crucial ecotone that supports a variety of biological communities and ecological processes. This zone serves as a refuge for aquatic organisms and plays a significant role in nutrient cycling and the transformation of organic matter (Brunke and Gonser, 1997; Ellis et al., 2007). River-aquifer exchanges affect the distribution and abundance of aquatic species by creating habitats with stable temperatures and nutrient availability (Brunke and Gonser, 1997; Krause et al., 2012).

These exchanges facilitate the natural attenuation of contaminants such as nitrates through denitrification processes in the hyporheic zone. This is particularly important for maintaining water quality in the river and the adjacent aquifer (Bartsch et al., 2014; Macdonald et al., 2018). The riverbed's permeability and organic-rich sediments' presence enhance the biogeochemical transformations that reduce pollutant concentrations (Brunke and Gonser, 1997; Macdonald et al., 2018).

Human activities, including GW extraction and the implementation of river management infrastructures, can significantly impact natural exchange processes. These interventions can result in diminished connectivity, modification of flow regimes, and potential degradation of water quality (Ellis et al., 2007; Jasechko et al., 2021). Aggravated with anthropogenic activities, climate change has an adverse impact on the hydrological regime of a river basin, leading to flooding events in the rainy season and dried channels in the lean season (Gaur et al., 2023). Increased rainfall intensity often leads to more surface runoff and less infiltration, reducing GW recharge (Jan et al., 2007). In India, the impact of rainfall intensity on GW recharge varies by region. In the northwest and north central regions, low-intensity rainfall is more beneficial for recharge, whereas in South India, high-intensity rainfall drives recharge.(Asoka et al., 2018). This reduced recharge and increased GW extraction lead to a declining GW trend, diminishing the baseflow to the GW-fed rivers. (Cooper et al., 1995; Mukherjee et al., 2018).

Managed aquifer recharge (MAR) and other interventions can be used to mitigate climate and human-induced impacts by enhancing GW storage and maintaining streamflow during critical periods (Ronayne et al., 2017). Before implementing appropriate artificial recharge measures, it is crucial to evaluate the current status of base flow and its future changes under potential climate change scenarios. The initial assessment for MAR implementation is a crucial task, which involves evaluating water source availability, GW

deficiency, and aquifer characteristics to select a suitable site (Dillon et al., 2019; Kumar et al., 2024; Pyne, 2017).

The assessment of water availability and its future requires a multi-faceted approach, involving the quantification of hydrological and GW fluxes at local and regional levels in the study area (Dillon et al., 2019). Evaluating the implications of climate change on water availability within a basin necessitates the employment of sophisticated hydrological modelling techniques, including SWAT and MODFLOW (Raju and Kumar, 2018). This assessment demands a comprehensive consideration of varied climate scenarios and a thorough understanding of the regional hydrological responses to these changes (Ahmed et al., 2022; Andréasson et al., 2004; Cooper et al., 1995; Mensah et al., 2022). The integrated modelling of SW (SW) and GW (GW), coupled with the simulated weather outputs of Global Climate Models (GCM), are widely incorporated to simulate the hydrological and GW fluxes based on the IPCC (Intergovernmental Panel on Climate Change) scenarios (Ahmed et al., 2022; Ali et al., 2020; Andréasson et al., 2004; Gaur et al., 2023; Mensah et al., 2022; Taylor et al., 2013).

Climate change has a profound impact on hydrological processes, particularly in arid regions with limited water resources. Rising temperatures and shifting precipitation patterns are key drivers of variability in baseflow and streamflow. Higher temperatures generally increase evapotranspiration, leading to reduced baseflow, while changes in precipitation can either mitigate or amplify these effects, depending on regional conditions (Hu et al., 2023b; Li et al., 2021; Miller et al., 2021; Xiang et al., 2021). Baseflow is particularly sensitive to climatic variables, exhibiting notable variability in response to temperature and precipitation changes (Hu et al., 2023b; Miller et al., 2021; Tan et al., 2020). Human activities, such as irrigation and water extraction, exacerbate the impacts of climate change, often reducing baseflow and altering streamflow (Huo et al.,

2008). These effects also vary seasonally and spatially, with some regions experiencing increased streamflow during wetter months and reduced baseflow during drier periods (Hu et al., 2023b, 2023a). Hydrological models predict that future climate scenarios will lead to more frequent and severe droughts, altering the timing and magnitude of peak stream flows (Miller et al., 2021; Xiang et al., 2021; Zhang et al., 2022). This underscores the need for region-specific water management strategies to address the challenges of climate change.

The baseflow or cumulative river aquifer exchanges (RAE), the portion of streamflow that originates from GW discharge, is a critical component in hydrological studies. The quantification of RAE is generally done by various analytical and empirical methods based on the observed stream flow data. These methods include recursive digital filters, conductivity mass balance (CMB), and various algorithmic approaches. For example, the recursive digital filter (RDF) method, when calibrated with the CMB method, has been shown to provide reliable long-term baseflow estimates (Zhang et al., 2013). With the advent of high computational availability, transient GW models have been used to simulate physical processes governing the interaction between SW and GW. These models can account for complex hydrological conditions and provide detailed insights into baseflow dynamics. For instance, a study using a fully integrated SW-GW flow model demonstrated that simulated baseflow could serve as a control experiment to evaluate the accuracy of automated baseflow separation methods (Partington et al., 2012). Another study highlighted the importance of considering bank storage effects in numerical GW models to accurately simulate baseflow, especially under varying hydrological conditions (Chen et al., 2006). Although the GW models are complex and require detailed input data, including hydrological, geological, and meteorological information (Chen et al., 2006), the methodology is widely applicable and

is suitable for detailed hydrological studies and scenarios where high accuracy is required (Chen et al., 2006; Partington et al., 2012). Further, due to limited streamflow data availability, the baseflow separation methods cannot be used in many cases. The methodology used to assess the impact of climate change on the RAE is generally achieved with the baseflow separation method, and none of the authors has used the integrated SW-GW model to the best of our knowledge. The accurate estimates of the GW models in simulating the RAE are crucial to seeing the impact of climate change on a small river like Varuna.

The RAE flux in small rivers is relatively low and generally not detectable by seepage meters. This makes it difficult to get accurate estimates of RAE, in the heterogeneous aquifer mediums (Tang et al., 2017, 2015). The well calibrated GW models are used by several researchers to simulate the reach scale RAE (Bajpai et al., 2022; Baratelli et al., 2016; Vergnes and Habets, 2018). However, these models are generally calibrated using GW heads which makes the estimated RAE uncertain. The differential flow gauging (DFG) is a method to directly measure the stream flow accretion between a river segment (Mccallum et al., 2012). These transient DFG measurements combined with tracer and thermal data has been widely used to determine the reach scale RAE (McCallum et al., 2014, 2012; Mccallum et al., 2012). The data from DFG has not been used to calibrate a numerical model as best of the authors knowledge and specially never used for a small river in Indian subcontinent.

Based on the research gap mentioned above, the integrated modelling-based impact of climate change on the RAE has been formulated. The hydrological fluxes in VRB were simulated using the SWAT model. The hydrological variables of SWAT have been integrated with the MODLFOW-NWT model and calibrated with observed GW heads and DFG data. The weather outputs of four scenarios (SSP126, SSP245, SSP370, and

SSP585) from CMIP6 models have been used to simulate future SW and GW fluxes with the integrated model. This chapter provides an accurate, physical model-based method to estimate current and future water resource availability in any small to large-scale river basin. The specific objectives of this chapter are as follows:

i. Calibration of heterogeneous aquifer properties and stream flow in the integrated SW-GW model
ii. Bias correction of temperature and precipitation from CMIP6 models
iii. Climate change impact assessment on RAE
iv. Analysis of future water availability in VRB

5.2 CMIP6 OUTPUTS AND ITS BIAS CORRECTION

The sixth phase of Coupled Model Intercomparison Projects (CMIP) is now available with daily simulation output of 58 General Circulation Models (GCMs) across the globe. Regarding the number of modelling organizations' participation, the number of future scenarios considered, and the number of different experiments undertaken, CMIP6 (Eyring et al. 2016) marks a significant increase over CMIP5. CMIP6 future climate forecasts include enhanced emissions, improved model parameterization, land use scenarios, and physical processes, among other things, all driven by scenarios based on shared socioeconomic paths (SSPs) (Eyring et al. 2016). In the simulation of distinct climate variables in different regions, CMIP6 GCMs have shown both better and worse performance than CMIP5. The performance of CMIP6 and CMIP5 in simulating the Indian summer monsoon rainfall was inconsistent in a comparative study by(Gusain et al., 2020). However, the performances of CMIP6 models in the simulation of global

temperature extremes, diminishing precipitation and droughts have been found to be superior (Rivera and Arnould, 2020).

Forecasts from climate models have been coupled with hydrologic models to estimate the potential consequences of climate change on water systems (Mohammed et al., 2015). Recently, (Muto et al. (2022) used an ensembled climate dataset to the SWAT (Soil & Water Assessment Tool) model to quantify the climate change impact on the hydrology of the Tokoro River Basin. (Kumar et al., 2022) studied the climate impact on the upper Betwa River catchment with the SWAT model and found a decrease in the annual rainfall and surface runoff for all scenarios. In India, the SWAT model has been used extensively with downscaled GCM data to study the impact of climate change on the hydrology of a basin (Sharannya et al., 2018). All these studies show a notable increase in rainfall intensity in the monsoon period and an increase of 1 °C–3 °C in the air temperature.

Since the GCM model outputs have a coarse spatial resolution and contain biases, they cannot be directly integrated with the SWAT model for hydrological applications. The statistical and dynamic modeling method generally performs the downscaling of GCM outputs. Statistical downscaling establishes empirical relationships between large-scale atmospheric and local climate variables, often using regression models, weather generators, and machine learning algorithms (Anandhi et al., 2008; Chen et al., 2012; Schmidli et al., 2006). Methods such as Relevance Vector Machine (RVM) and Support Vector Machine (SVM) have been used to model streamflow and other hydrological variables at finer scales (Anandhi et al., 2008). Dynamical downscaling uses higher-resolution regional climate models (RCMs) driven by GCM outputs to simulate local climate conditions more accurately. This method is computationally intensive but provides detailed regional climate information, which is crucial for climate adaptation planning.

Recently, a new global bias-corrected, high-resolution (0.25° × 0.25°), statistically downscaled product, known as the National Aeronautics and Space Administration (NASA) Earth Exchange Global Daily Downscaled Projections (NEX-GDDP) dataset (Thrasher et al., 2012) has been provided by NASA. NEX-GDDP demonstrates several advantages over CMIP5 and CORDEX data in simulating the Indian Summer Monsoon. It provides higher accuracy in spatial patterns, reduced errors, better simulation of inter-annual variations, and more realistic extremes (Jain et al., 2019). Additionally, it performs better in seasonal temperature and precipitation simulations and offers an improved representation of aerosol effects (Singh et al., 2019). These strengths make NEX-GDDP a valuable tool for future projections and climate change impact studies in the study area.

Table 5.1. GCM Models

S/N	Models	Spatial Resolution	Institution
1	ACCESS-CM2	1.875° × 1.25°	Australian Community Climate and Earth-System Simulator
2	ACCESS-ESM1-5	1.875° × 1.25°	Australian Community Climate and Earth-System Simulator
3	BCC-CSM2-MR	1° × 1°	Beijing Climate Center
4	CanESM5	2.81° × 2.79°	Canadian Earth System Model
5	CMCC-ESM2	0.9° × 1.25°	Euro-Mediterranean Centre on Climate Change
6	CNRM-CM6-1	1.41° × 1.40°	National Centre for Meteorological Research, France
7	EC-Earth3-Veg-LR	1° × 1°	EC-Earth consortium, Rossby Center, Swedish Meteorological and Hydrological Institute/SMHI, Norrkoping, Sweden
8	EC-Earth3	1° × 1°	EC-Earth consortium, Rossby Center, Swedish Meteorological and Hydrological Institute/SMHI, Norrkoping, Sweden
9	FGOALS-g3	1° × 1°	Chinese Academy of Sciences, Beijing, China
10	GFDL-ESM4	1° × 1°	National Oceanic and Atmospheric Administration, Geophysical Fluid Dynamics Laboratory, Princeton, NJ, USA
11	GISS-E2-1-G	2.5° × 2°	Goddard Institute for Space Studies (GISS), New York, NY, USA
12	INM-CM4-8	2° × 1. 5°	Institute for Numerical Mathematics, Russia
13	INM-CM5-0	2° × 1. 5°	Institute for Numerical Mathematics, Russia
14	MIROC-ES2L	4.5° × 4. 5°	Japan Agency for Marine-Earth Science and Technology (JAMSTEC), Kanagawa, Japan, Atmosphere and Ocean Research Institute (AORI), The University of Tokyo, Chiba, Japan, National Institute for Environmental Studies (NIES), Ibaraki, Japan, and RIKEN Center for Computational Science, Hyogo, Japan (MIROC)
15	MIROC6	1.41°×1.40°	Atmosphere and Ocean Research Institute (The University of Tokyo), National Institute for Environmental Studies, and Japan Agency for Marine-Earth Science and Technology, Japan
16	MPI-ESM1-2-HR	1.88° × 1.86°	Max Planck Institute for Meteorology, Germany

17	MPI-ESM1-2-LR	1.88° × 1.86°	Max Planck Institute for Meteorology, Germany
18	MRI-ESM2-0	1.13° × 1.12°	Meteorological Research Institute, Japan
19	NorESM2-LM	2.50° × 1.89°	Norwegian Climate Center, Norway
20	NorESM2-MM	2.50° × 1.89°	Norwegian Climate Center, Norway
21	TaiESM1	0.9° × 1.25°	Research Center for Environmental Changes, Academia Sinica, Nankang, Taipei, Taiwan

The data from the NCCS THREDDS (https://www.nccs.nasa.gov/services/data-collections/land-based-products/nex-gddp-cmip6) has been downloaded for 21 best-performing models (**Table 5.1**), which has been previously applied in hydrological applications (Gusain et al., 2020; Hemanandhini and Vignesh Rajkumar, 2023; Kamruzzaman et al., 2021). The target variable for the bias correction is the 2D gridded data from IMD. We used the Random Forest Regressor (RFR) to bias-correct the maximum and minimum temperature variables using 'tasmax' and 'tasmin' as independent variables, and IMD temperature data as dependent variables. The precipitation data from GCM models was bias-corrected using an LSTM model. We chose the algorithms based on their accuracy and computational requirements. The RFR requires lower computational resources compared to LSTM and has shown accurate predictions for temperature variables. On the other hand, precipitation data requires LSTM due to its high randomness and non-linearity. The LSTM has shown high accuracy compared to RFR and other algorithms in various research studies.

Table 5.2. GCM Models accuracy w.r.t to IMD 2D Gridded data (the bolded font has been used to represent selected models)

		Variables					
		pr (mm)		tasmax (°C)		tasmin (°C)	
S/N	Models	R2	RMSE	R2	RMSE	R2	RMSE
1	ACCESS-CM2	0.09	114.57	0.84	2.11	0.93	1.73
2	ACCESS-ESM1-5	0.06	116.86	**0.86**	2.02	0.94	1.64
3	BCC-CSM2-MR	**0.48**	86.93	**0.86**	1.99	**0.95**	1.42
4	CanESM5	0.27	102.8	0.83	2.19	0.93	1.72
5	CMCC-ESM2	**0.35**	97.15	0.83	2.2	0.93	1.69
6	CNRM-CM6-1	**0.31**	100.23	0.81	2.32	**0.95**	1.5

7	EC-Earth3-Veg-LR	**0.35**	97.27	0.83	2.22	**0.95**	1.49
8	EC-Earth3	0.29	101.66	0.83	2.17	0.94	1.61
9	FGOALS-g3	0.28	102.46	**0.85**	2.03	0.94	1.57
10	GFDL-ESM4	0.28	102.42	**0.85**	2.04	0.94	1.65
11	GISS-E2-1-G	0.17	109.97	**0.85**	2.04	0.92	1.84
12	INM-CM4-8	0.15	110.75	0.84	2.16	**0.95**	1.5
13	INM-CM5-0	0.24	104.61	**0.85**	2.09	**0.95**	1.48
14	MIROC-ES2L	**0.49**	85.61	**0.85**	2.05	**0.96**	1.37
15	MIROC6	**0.37**	95.53	0.83	2.17	**0.95**	1.41
16	MPI-ESM1-2-HR	**0.47**	87.82	0.84	2.11	0.93	1.72
17	MPI-ESM1-2-LR	**0.37**	95.47	0.82	2.23	0.93	1.68
18	MRI-ESM2-0	0.19	108.25	**0.85**	2.08	0.94	1.57
19	NorESM2-LM	0.28	101.8	**0.86**	1.99	**0.95**	1.53
20	NorESM2-MM	**0.36**	96.27	**0.85**	2.04	0.92	1.84
21	TaiESM1	**0.31**	99.8	0.64	3.2	-0.87	8.94

The performance of each climate model was initially evaluated by comparing its R^2 score and RMSE against IMD data at each grid location. After screening 21 models, the ten most accurate ones were chosen and combined to calculate the average of all climate variables across four scenarios (SSP126, SSP245, SSP370, and SSP585). The models were trained using historical data from the average dataset, and predictions were made for future scenarios at all grid locations within the study area. The accuracy of the bias-corrected variables is illustrated in the **Figure 5.1** to **Figure 5.3**. The average projected climate variables have been plotted in **Figure 5.4** along with the variation over all the study area.

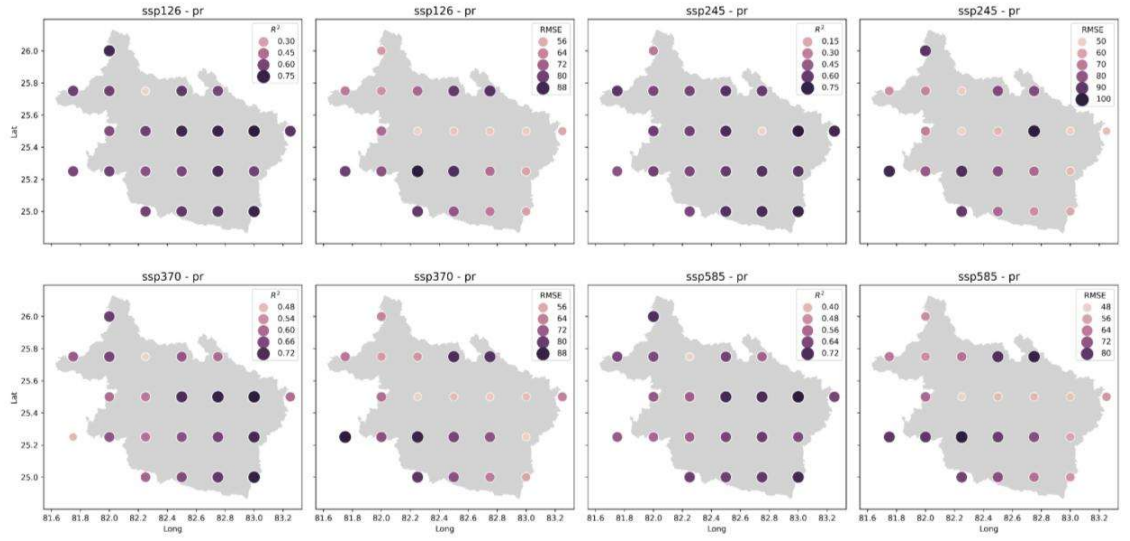

Figure 5.1. *R^2 scores and RMSE across all scenarios of the LSTM model for bias correction of precipitation.*

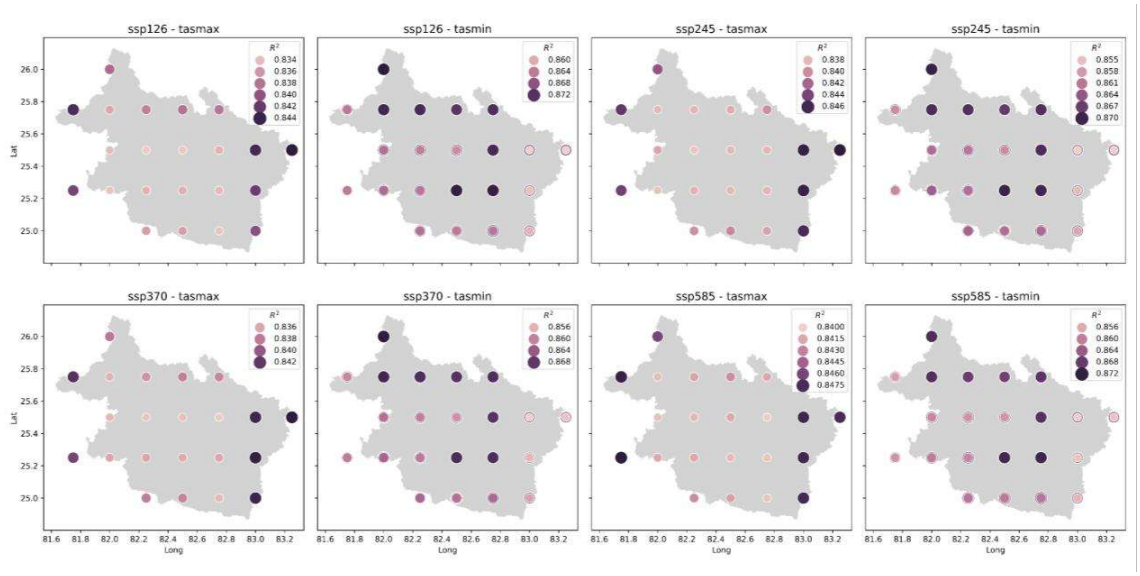

Figure 5.2. *R^2 scores across all scenarios of the RFR model for bias correction of temperature.*

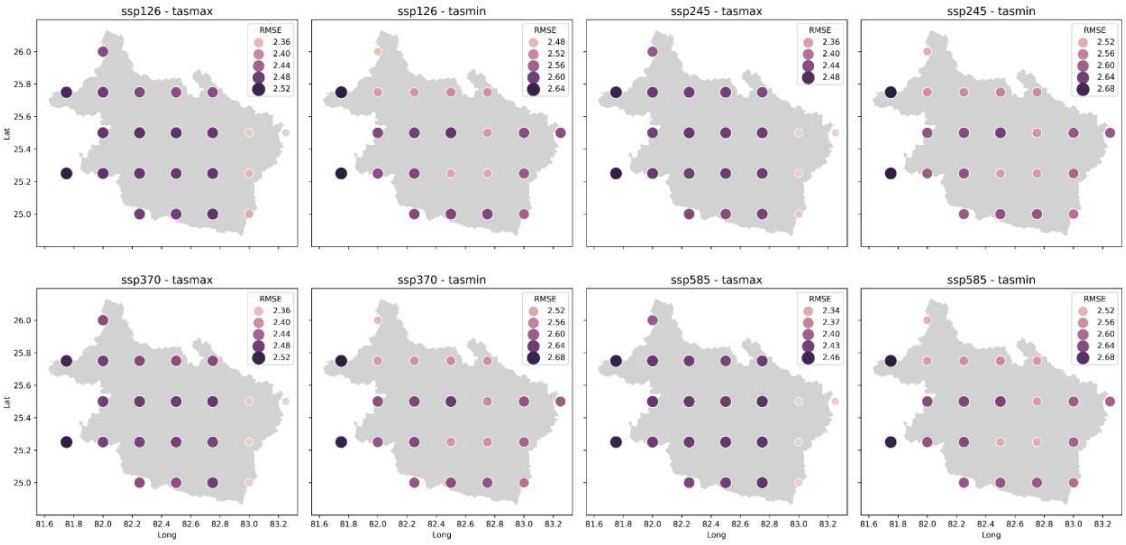

Figure 5.3. *RMSE scores across all scenarios of the RFR model for bias correction of temperature*

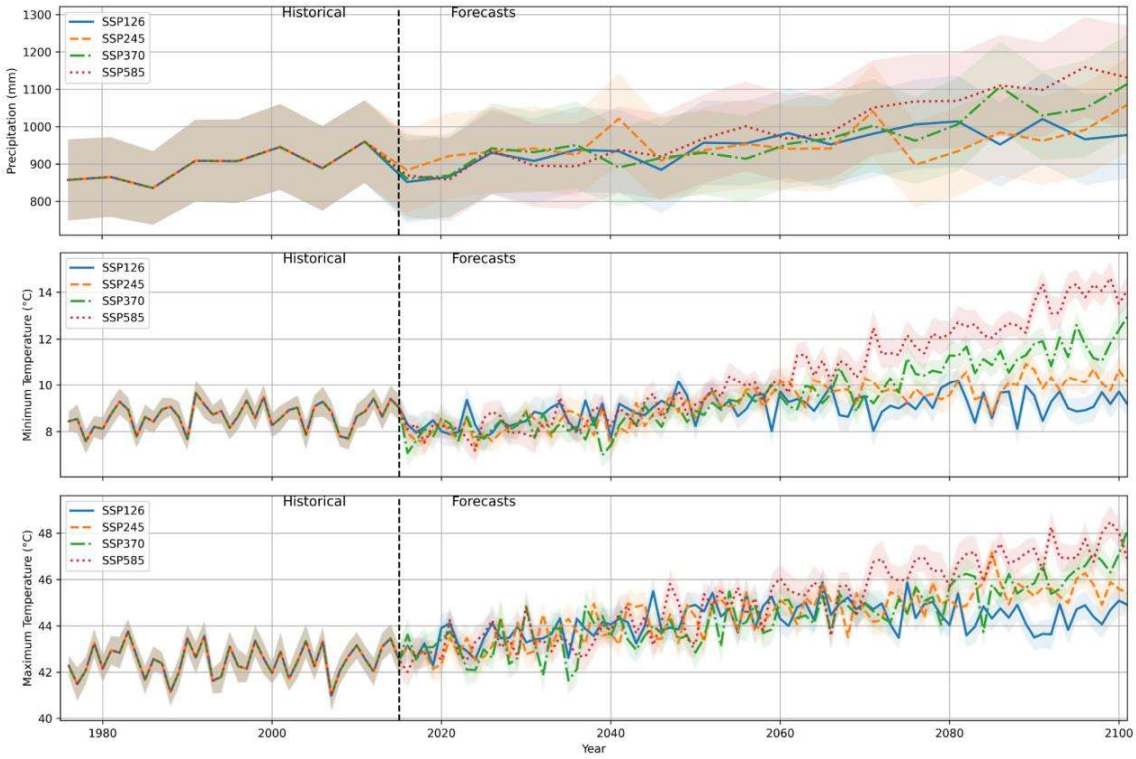

Figure 5.4. *The projected climate variables in VRB (The data has been plotted as annual averages to create smooth plots. The precipitation data is 5-year average data, and temperature data are annual minimum or maximum.)*

5.3 MODELLING THE SW DYNAMICS IN VRB

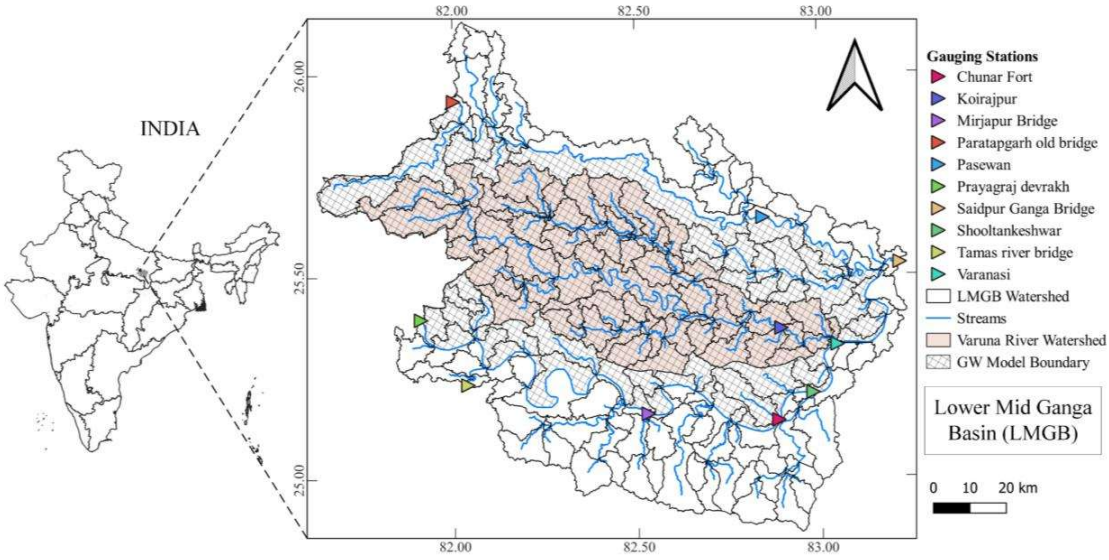

***Figure 5.5**. Modeled area and discharge measurement locations*

5.3.1 Dataset

Various datasets used for the modelling of LMGB have been discussed below.

1. ***Topography***: The elevation data required for the stream and watershed delineation has been taken from SRTM 1 arc second (approx. 30 meter) Digital elevation model (DEM).
2. ***Land Use***: The land use data for LMGB has been developed with the help of Landsat 8 Products. The imagery has been classified into five major land use classes with the help of Random Forest classification(Breiman, 2001). The training dataset has been prepared manually and ground truthing has been done on the field. The classification category and their subclasses has been discussed below.
    a. *Agriculture area*: This class includes the area which are cultivated and fallow land.
    b. *Built up*: This class includes residential and industrial buildings as well as transportation systems. All other impervious area has been classified in this category.

c. *Water Body*: The water body consists of rivers, streams, canals (width greater than 30 meters), dams and ponds (size greater than 900 m^2).

d. *Vegetation*: This category includes all the green areas with large to small trees and shrubs.

e. *Bare soil/sand*: In this category the bare earth with highest probability of percolation has been classified, which includes bare soil, geological outcrops, and sand bars in the river.

3. ***Soil***: The soil map and its properties have been taken from the Harmonised World Soil Database (HWSD), which has been developed by the Food and Agriculture Organization (FAO) of the United Nations. The saturated hydraulic conductivity for all soil types has been calibrated after modelling with the HWSD data. It is found that the original values have been increased to 3.47 times to fit the observed discharges better (**Table 5.4**).

Table 5.3. Soil properties as per FAO Classification (HYDGRP: Soil hydrologic group based on its infiltration characteristic, SOL_Z: Soil Depth in mm, SOL_BD: Soil Bulk Density, SOL_AWC: Available water content, SOL_K: Saturated hydraulic conductivity, SOL_CBN: Amount of organic carbon in the layer (%), CLAY: Percentage of clay, SILT: Percentage silt in soil, SAND: Sand percentage in soil, ROCK: Percentage of rock mass in soil, SOL_ALB: Moist soil albedo, USLE_K: USLE soil erodibility factor).

SNAM (FAO)	Layer	HYDGRP	TEXTURE	SOL_Z (mm)	SOL_BD (g/cc)	SOL_AWC (%)	SOL_K	SOL_CBN	CLAY (%)	SILT (%)	SAND (%)	ROCK (%)	SOL_ALB	USLE_K
Be74-2a-3675	1	C	LOAM	300	1.2	0.16	13.63	1.1	22	36	42	0	0.06	0.29
	2			1000	1.1	0.16	21.35	0.6	24	35	40	0	0.15	0.29
Be84-2a-3685	1	D	LOAM	300	1.3	0.18	8.31	1.2	22	37	41	0	0.05	0.29
	2			1000	1.2	0.18	12.57	0.5	25	36	38	0	0.19	0.29
Lc5-1a-3772	1	D	SANDY CLAY LOAM	300	1.5	0.16	8.14	0.4	24	17	59	0	0.23	0.23
	2			1000	1.6	0.16	3.2	0.3	34	16	50	0	0.27	0.23
Lf10-1bc-3785	1	C	SANDY LOAM	300	1.5	0.14	19.13	0.6	14	15	71	0	0.15	0.24
	2			1000	1.4	0.14	13.66	0.3	26	14	61	0	0.27	0.24
Lo51-2a-3812	1	D	LOAM	300	1.4	0.18	6.87	0.8	22	32	47	0	0.10	0.29
	2			1000	1.4	0.18	4.71	0.3	29	31	41	0	0.27	0.29

4. ***Weather data***: SWAT requires various atmospheric parameters to simulate the evapotranspiration for a given rainfall based on the physical model used. Generally, Hargreaves or Penman-Monteith equations is used for the calculation of potential evapotranspiration (PET). The actual evapotranspiration (AET) is calculated as a fraction of PET which depends on the land cover, soil moisture and

plant growth conditions. Hargreaves method is based on temperature (maximum and minimum) data only, which makes it widely applicable (Itenfisu et al., 2003) as most of the weather stations has temperature data specially for arid and semi-arid regions (Droogers and Allen, 2002; Saghravani, 2009). Daily rainfall and temperature data for the study area has been prepared from IMD 2D gridded data (Pai D.S. et al., 2014).

5. ***River discharge measurements***: The SWAT was developed to simulate large-scale ungauged watersheds with minimal calibration efforts and can provide satisfactory results (Qi et al., 2020). Although the results can be satisfactory without the calibration, it is essential to calibrate the model with observation data to reduce the uncertainty due to human interventions. The river discharge data has been collected for the January 2021 to December 2023 with Advance Dopler Current Profiler (ADCP) with temporal resolution of 10 to 30 days on Ten cross sections (Six on Ganga, one on Varuna, one on Tons and two on Gomati River). The data has been converted to daily observation with river stage and discharge relationship. The daily stage has been observed with DGPS.
6. ***Evapotranspiration***: The 500m MOD16A2GF product derived from MODIS data has been used to generate the subbasin scale mean evapotranspiration time series with temporal resolution of 8 days.

5.3.2 Simulation

The model has been setup in the ArcGIS environment with ArcSWAT plugin. The DEM has been filled for sinks, prior to stream delineation. The outlets for the five gauging stations for calibration have been created manually and three for the inlet discharge (**Figure 5.5**). The hydrologic response units (HRUs) have been delineated by overlaying the soil, land use and slope maps. The temperature and rainfall data has been formatted for weather generator with python and imported into the model. The inlet discharge data has been formatted and imported as per required format of txt file. The model has been simulated for five years (January 2020 to December 2023) with one years as warmup period.

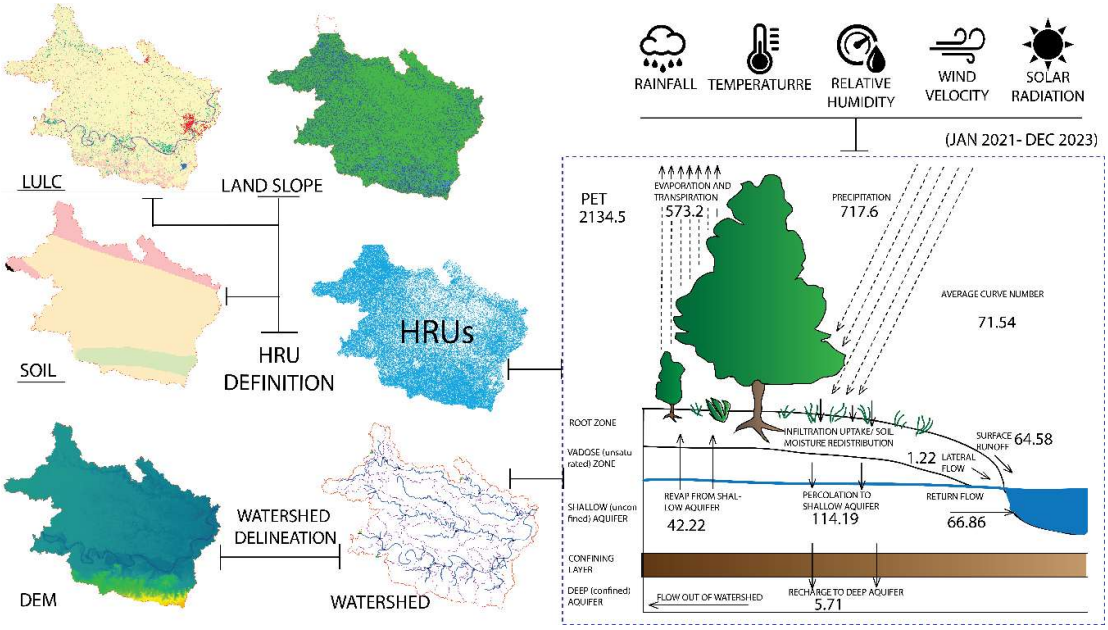

***Figure 5.6**. SWAT Model of Lower Mid Ganga Basin*

5.3.3 Calibration and Validation

The model has been calibrated with daily discharge data from January 2021 to December 2022 on seven-gauge stations and three subbasin evapotranspiration (MODIS 500m ET) with Sequential Uncertainty Fitting (SUFI-2) (Abbaspour, 2019) algorithm in R-SWAT using Nash-Sutcliffe efficiency (NSE) as the objective function. The 24 parameters have been selected based on previous studies (Aliyari et al., 2019; Anand et al., 2021; Shivhare et al., 2018) conducted on the middle Ganga basin and based on unknown variables in the model. The sensitivity analysis has been performed, and the twelve most sensitive parameters have been chosen to be calibrated (**Table 5.4**). The curve number has been the most sensitive parameter, followed by the runoff lag time and evaporation compensation factor. The lateral flow travel time has also been a sensitive parameter which has been added for calibration to manage the high lateral flow which has been observed in the default simulation. Multiple sets of the calibrated parameters have shown a good correlation with the observed data. The variation of the parameters has been analysed by

determining the 95 per cent prediction uncertainty (95PPU). The upper (97.5 percentile) and lower bound (2.5 percentile) of fitted parameters have been calculated by fitting the suitable probability distribution function for each set of parameter values. The best parameter set was chosen based on the site characteristics and field experience.

Table 5.4. SWAT Parameters and their calibrated values. The parameters have been arranged based on their sensitivity in the form of rank. The suffix for the parameters represents the method of changing values during calibration (A:- added by r, R:- multiplied by 1+r, V:- Replaced by r, while r is the fitted value)

Rank	Parameter	Description (Method: A-Absolute; R-Relative;V-Replace)	Lower (95PPU)	Median	Upper (95PPU)	Best Parameters
1	CN2.mgt	*SCS runoff curve number --R*	-0.19	-0.17	-0.09	-0.18
2	SURLAG.hru	*Surface runoff lag time --V*	0.51	1.67	6.35	1.03
3	ESCO.hru	*Soil evaporation compensation factor --V*	0.56	0.70	0.79	0.75
4	LAT_TTIME.hru	*Lateral flow travel time --R*	4.63	26.83	46.56	24.89
5	SURLAG.bsn	*Surface runoff lag time --V*	3.13	4.57	5.75	4.24
6	ALPHA_BNK.rte	*Baseflow alpha factor for bank storage --V*	0.01	0.10	0.19	0.04
7	SOL_AWC.sol	*Available water capacity of the soil layer --R*	0.03	0.14	0.28	0.06
8	REVAPMN.gw	*Treshold depth of water in the shallow aquifer for "revap" to occur(mm) --V*	40.69	268.32	460.73	122.95
9	CH_K2.rte	*Effective hydraulic conductivity in main channel (Alluvium) --V*	0.05	0.25	0.45	0.18
10	SLSOIL.hru	*Slope length for lateral subsurface flow --R*	24.72	91.20	165.72	43.87
11	GW_DELAY.gw	*GW Delay (days) --A*	121.80	269.24	432.24	404.24
12	ALPHA_BF.gw	*Baseflow alpha factor for grundwater (days) --V*	0.04	0.17	0.34	0.13

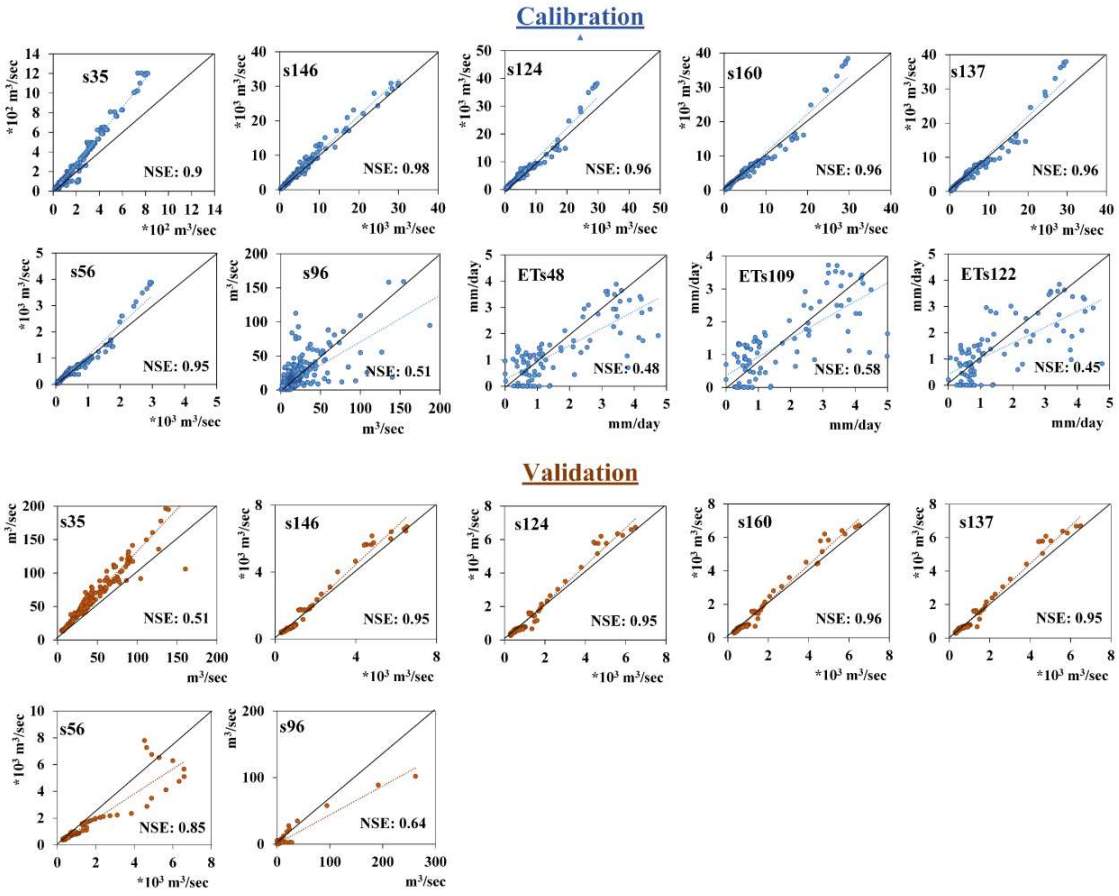

Figure 5.7. *Scatter plot of observed vs. Simulated variables of the calibrated model (s#: the subbasin number corresponding to the discharge gaging sites, ETs##: subbasin numbers corresponding to the subbasins that have been calibrated with MODIS ET data)*

5.4 GW MODELLING

The GW for the VRB has been modeled with MODFLOW-NWT using the conceptual model approach in GMS (Aquaveo). The modeling steps and data have been summarized below.

1. **Geology**: The VRB is characterized by quaternary older alluvium. The occurrence of newer alluvium is limited near Varanasi and along the Ganga River. According to the lithology, the older alluvium consists of Silty Sand, Clayey Silt or Clayey Sand. The occurrence of calcrete (locally called Kanker) is also visible in different river reaches in the Varuna River.

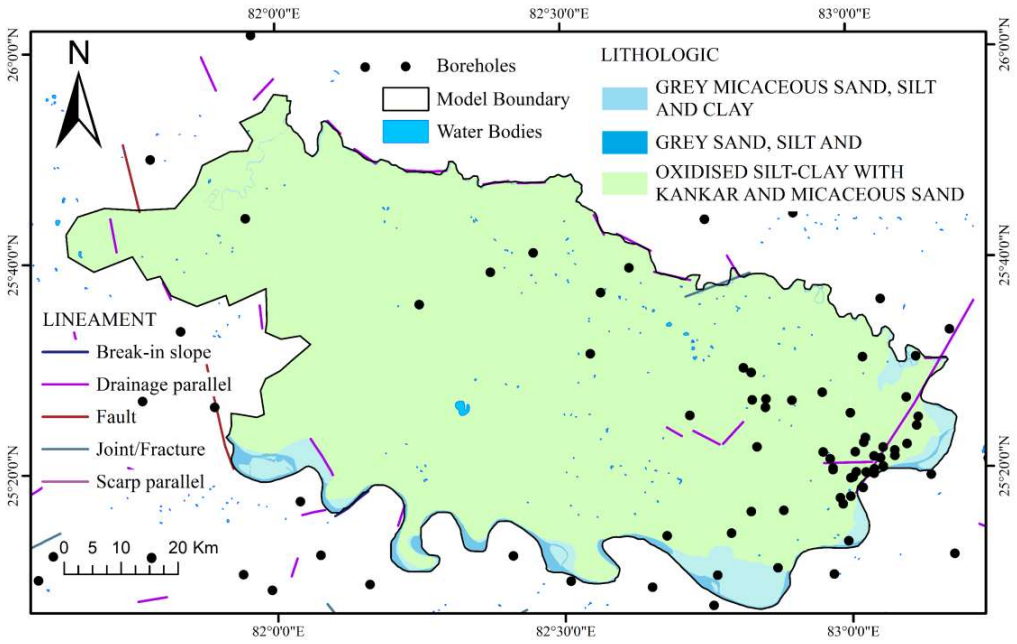

***Figure 5.8**. Lithological characterization of the modeled area*

The alluvial deposits of the early to middle Pleistocene period, which were deposited by the Gangetic River system, underlie the Doab between the Ganga and Gomati rivers. Near the Ganga floodplain, newer Holocene alluvium has been deposited on the weathered basement of the Upper Vindhyan formation, consisting of sand, silt, clay, and calcrete in varying proportions. Similarly, the right side of the Ganga River is underlain by Quaternary alluvium up to the foothills of the northern Vindhyan plateau (GSI). The Kaimur sandstone/quartzite of the upper Vindhyan formation can be found in masses and isolated hillocks in the southern part of the River Ganga.

2. **Aquifer properties**: The GW occurs in the pore spaces of unconsolidated alluvial sediments. Shallow aquifers contain GW under water table conditions, while deeper aquifers contain GW under semi-confined to confined conditions. Four aquifer groups have been mapped with the borehole drilling data, with aquitard layers of clayey silt in between **Figure 5.9**.

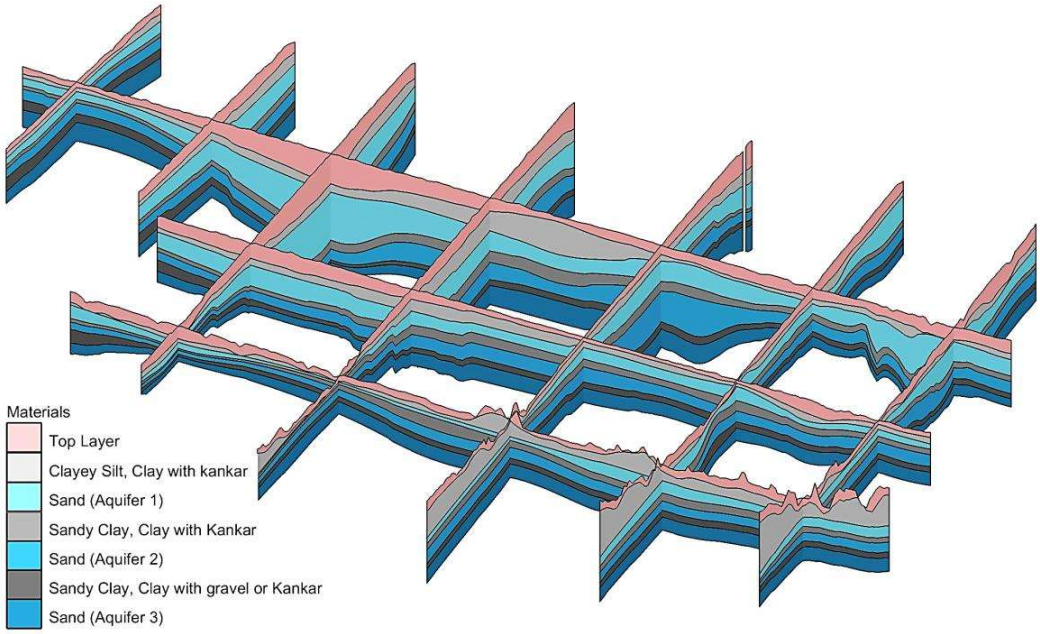

Figure 5.9. *Lithological fence diagram of the modelled area*

The top unconfined alluvium layer, which extends from 7.3 meters to 149.9 meters below ground level, generally consists of silty sand with kankar and has lower hydraulic conductivity. The clayey aquitard layers, with thickness varying from 4 meters to 114 meters, separate the aquifers. The aquifers are heterogeneous and found to have frequent occurrence of clay facies. Data from the NAQUIM report on the pumping test at around 30 sites suggests an average hydraulic conductivity (HK) of 130.7 m/day, 128.4 m/day, and 152.8 m/day for the 2nd, 3rd, and 4th aquifer, respectively. The minimum HK value was as low as 1.08 m/day to 1635.25 m/day, which manifests the high heterogeneity of the aquifer. The data of 18 test sites manifests average specific storage (Ss) of 0.00073, 0.00143, and 0.00166 for the 2nd, 3rd, and 4th aquifer, respectively. The minimum Ss is found to be $4.15 * 10^{-8}$ and the maximum of 0.0219.

3. **Conceptual Model**: The model has been conceptualized as a seven-layer system with different boundary conditions. Two types of perimeter boundary conditions

have been employed, such that the Gomati River and Ganga River form the general head boundary (RIV package) in the top layer of the model. The rest of the perimeter in all layers has been conceptualized as specified head boundaries (CHD package). The measured stage data of Gomati and Ganga from gaging stations at a temporal interval of 10-30 days has been assigned as node data.

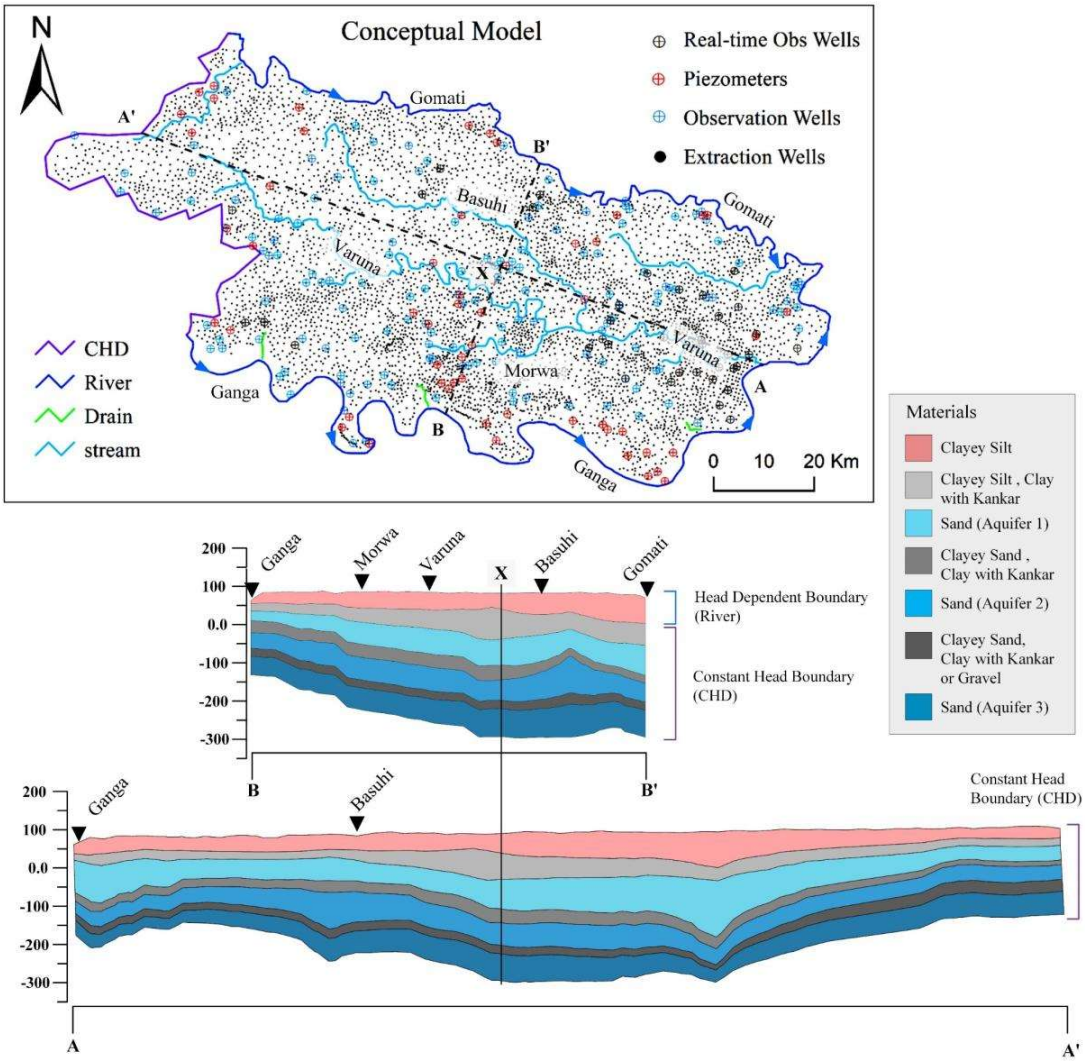

***Figure 5.10**. Conceptual model of the VRB with boundary conditions*

The stages are linearly interpolated between two nodes. The CHD boundary nodes have been selected based on the area's location of adjacent observation wells. The

daily GW level from digital water loggers (DWLR) from the GW department[4], Govt. of Uttar Pradesh, along with the seasonal GW table data from the WRIS portal[5], has been used to assign node data to the CHD package.

The sources, including the recharge and streams, and sinks, such as extraction wells, evapotranspiration, and streams, make the internal boundary conditions in the model. The Varuna River flows in the middle of the modelled area and is conceptualised with 57 segments based on the watershed outlets and DFG locations. The river bed elevations and river cross-section have been measured with DGPS[6] and ADCP[7]. The mean bed slope of Varuna River has been determined to be 0.43 m/Km for the longest reach. The bed slope of the Basuhi River was 0.2 m/Km. The bed has shown negative slopes in many reaches, including pools and riffles in the Varuna.

The GW extraction wells were determined based on the number of towns and villages in the area. The number of wells per village or town has been increased based on the spread of built-up areas. This is to ensure that individual wells do not extract a high volume of GW to avoid depleting the water table. After finalizing the demands based on the methodology proposed in Chapter 3, a total of 5246 wells have been planned to address the water demand for domestic and irrigation

[4] https://upgwd.gov.in/StaticPages/WDMS_Login.aspx
[5] https://indiawris.gov.in/wris/#/
[6] Digital Geographic Positioning System
[7] Acoustic Doppler Current Profiler

uses (**Figure 5.10**). Apart from this, 49 seasonal observations and 18 monthly observation wells have been modeled, with a total of 556 observations.

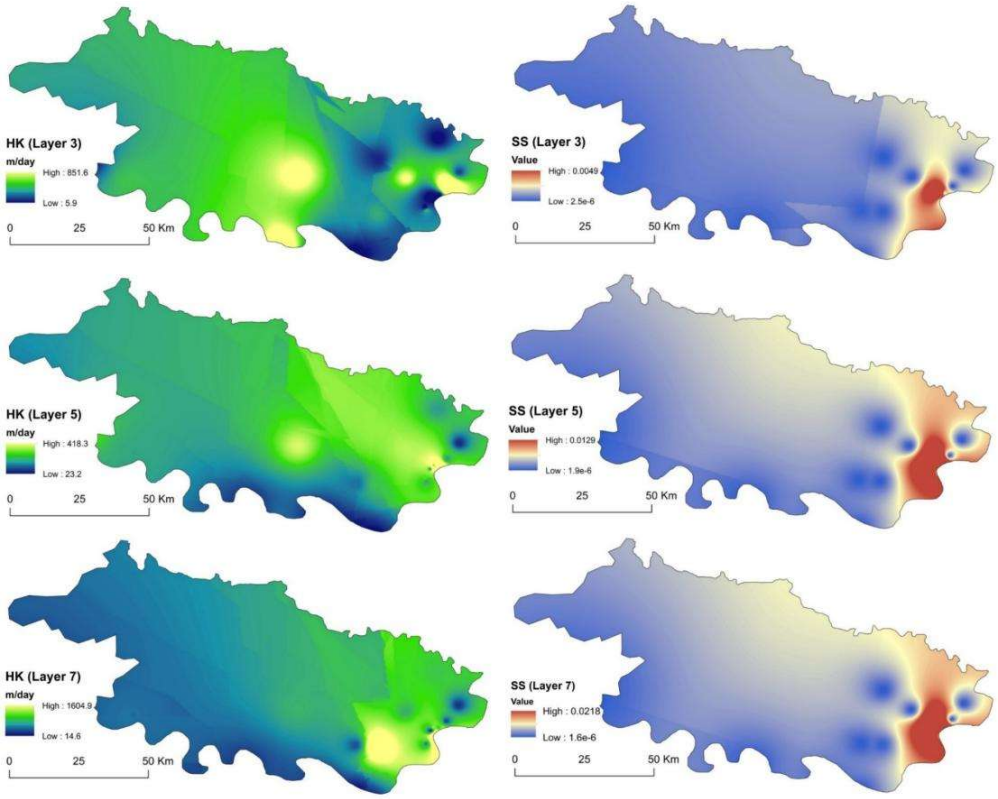

***Figure 5.11**. observed aquifer properties*

4. Translation to Numerical Model:

The conceptual model has been translated to relevant packages in MODFLOW-NWT, as discussed in Chapter 3. The model has been divided into square grids measuring 750m and 7 layers. Time has been divided into monthly time steps. GW extraction has been simulated using the WELL package, with the screen locations set to the 1st confined aquifer (3rd layer), as most pumping wells are located in this aquifer. The Varuna River has been modeled using the SFR2 package to estimate stream flow accurately. The GAGE package has been employed to monitor flow and stages during flow routing in SFR2. The stream

cross-section from the confluence of Basuhi and Varuna has been modeled using the eight-point method, as discussed in Chapter 3, while the rest of the stream cross-section has been modeled as a wide rectangular channel. Stream flow inputs, such as precipitation, evaporation, runoff, and reach inflow, have been obtained from the simulation outputs of the SWAT model. The evapotranspiration (EVT package) and recharge (RCH Package) have been calculated on a subbasin basis using SWAT simulations. Drain package (DRT) has been used to model the small streams.

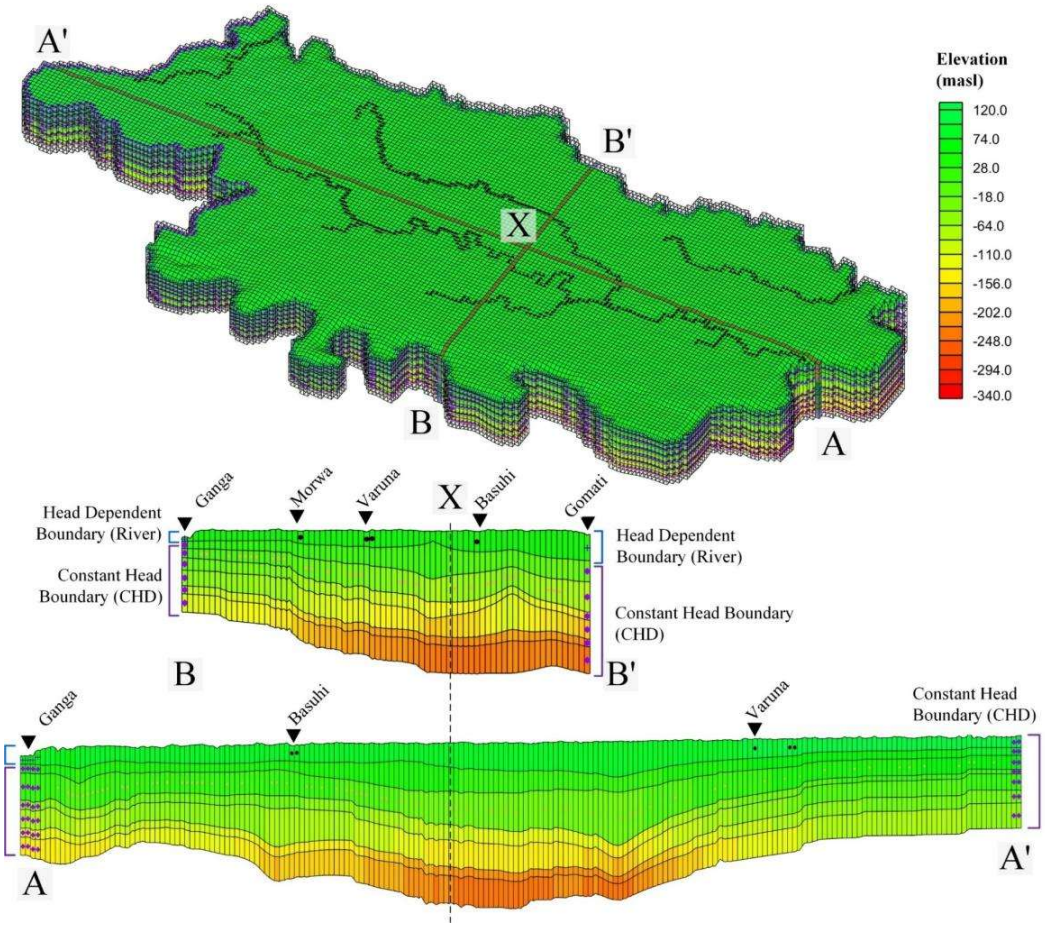

***Figure 5.12**. Numerical Model of the study area*

5.5 INTEGRATED MODELLING OF SW AND GW IN VRB

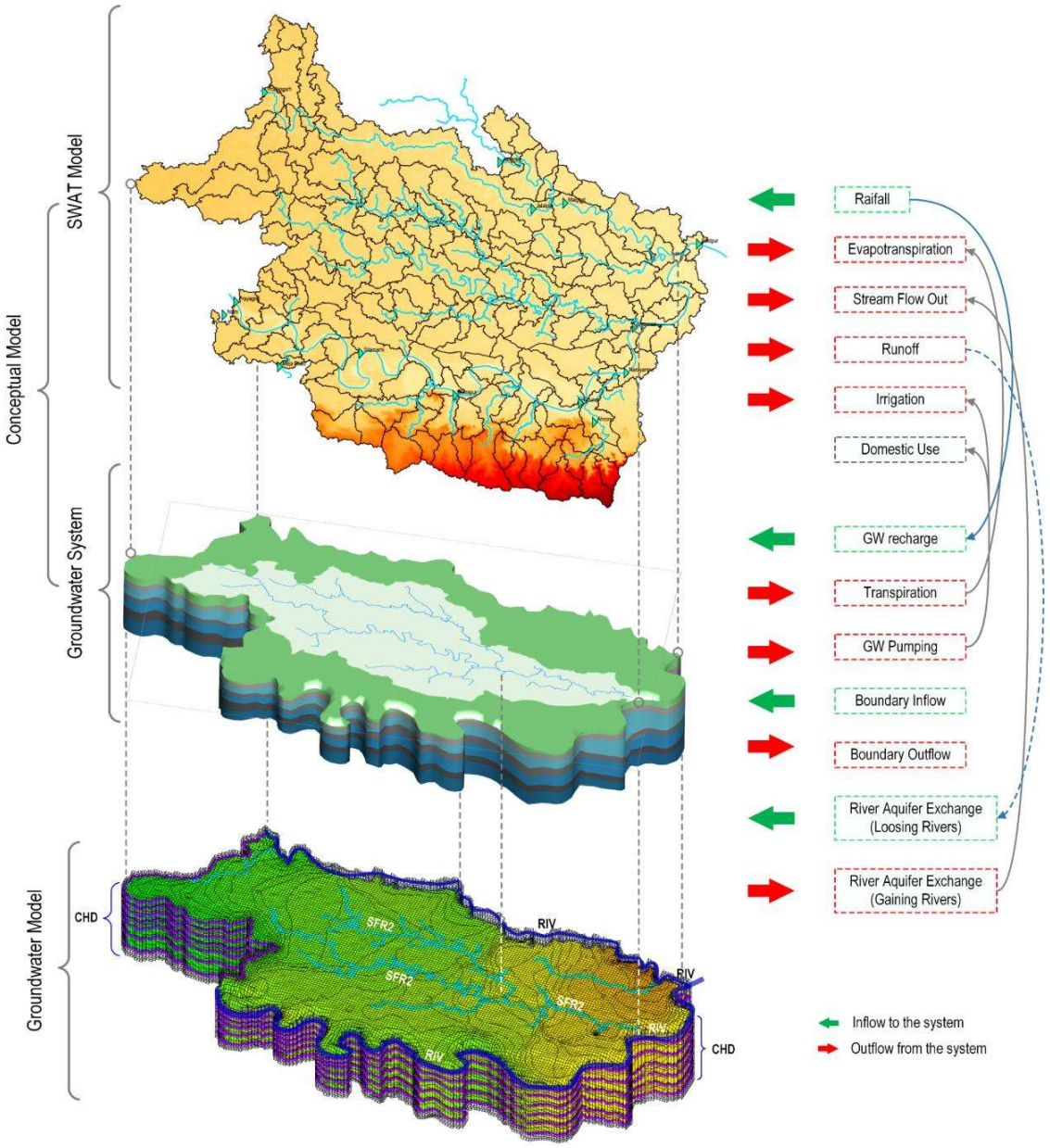

***Figure 5.13**. Integrated Model of VRB and GW system*

The GW and SW models have been integrated based on a loose couple approach, in which the outputs of the SWAT model have been used as input to the MODFLOW model. The EVT package and RCH package inputs have been taken from the HRU Outputs of SWAT, which have been resampled by the weighted area method to the basin scale. The stream

flow inflows, runoff, evaporation, and precipitation have been taken from the SWAT model's HRU output and RCH outputs based on defined reach lengths.

5.6 DIFFERENTIAL FLOW GAGING (DFG)

Differential flow gauging has been used to calculate the loss or gain of stream flow into the surrounding GW. The methodology is based on the water balance for the river reach:

$$Q_{in} + Q_t + Q_g = Q_{out} + Q_d + ET + \frac{\Delta S}{\Delta t} \quad 5.1$$

Where Q_{in} is inflow at the upstream of the reach, Q_t is the inflow from tributaries and point sources, Q_g is the GW flux to the river reach, Q_{out} is the outflow from the river reaches at the downstream end, Q_d is the flow out from the reach due to diversions and canal feeder pumps, *ET* is the evapotranspiration from the river reach, and $\frac{\Delta S}{\Delta t}$ is the change in river bank storage with time. All the components of the equation 5.1 has the unit of discharge (L^3T^{-1}).

In the case of no tributary and point sources in the study reach, the inflow and outflow components of the water balance are zero. The evapotranspiration along the river reach is generally much lower than the discharge. So, for this specific case, the seepage flux between two sections with total wetted area A_w is given as

$$RAE = \frac{Q_{out} - Q_{in}}{A_w} \quad (LT^{-1}) \quad 5.2$$

The discharge data for all eight locations named “VDP01 - 08” has been collected with ADCP for six lean flow periods in 2022 and 2023. The data collection has been performed

multiple times in the section to get three consecutive similar measurements to account for uncertainty due to collection method (misalignment during transaction and varying velocity) and field limitations (such as underwater flora and flow ripples). The ADCP has been properly calibrated and care has been taken to avoid local attractions for accurate functioning. The cross-sections and stream velocity distributions has been presented in **Figure 5.14**.

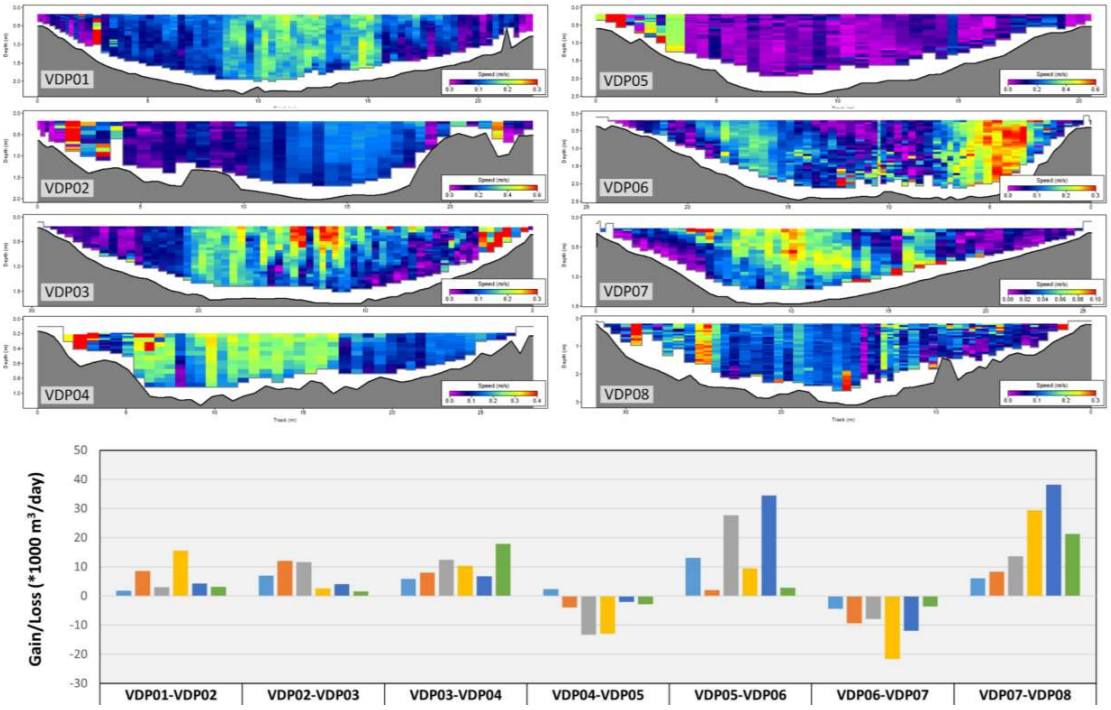

***Figure 5.14**. River cross-section and velocity profile, along with the net loss and gain for each stream segment*

5.7 CALIBRATING THE GW MODEL FOR RAE

The GW model has been calibrated with the observed GW heads and DFG data. The PEST algorithm has been used with the pilot point method, which has offered significant advantages in estimating hydraulic properties like hydraulic conductivity (K) and specific storage (S_s). This approach enhanced model flexibility by allowing for spatially variable parameter estimation across the model grid, which had been crucial in heterogeneous

aquifers. The pilot points have been uniformly distributed across the model grid with a distance of 5 Km. The known parameter values have been assigned, and those points have been fixed (parameter value has not been determined but is used for the interpolation). The parameter initial estimates have been taken from the observed data. By strategically placing pilot points, local variations were effectively captured. The iterative nature of PEST refined model predictions by minimizing RMSE between observed and simulated data, while regularization techniques (Tikhonov Regularization) stabilized the calibration process, making it possible to handle highly parameterized models without overfitting. A mean residual head of 1.05 meters, R^2 of 0.86, and RMSE of 2.88 have been achieved, representing a satisfactory calibration (**Figure 5.15**). the calibrated aquifer parameters can be found in Appendix B. The fitted conductivity range can be observed in **Figure 5.16**.

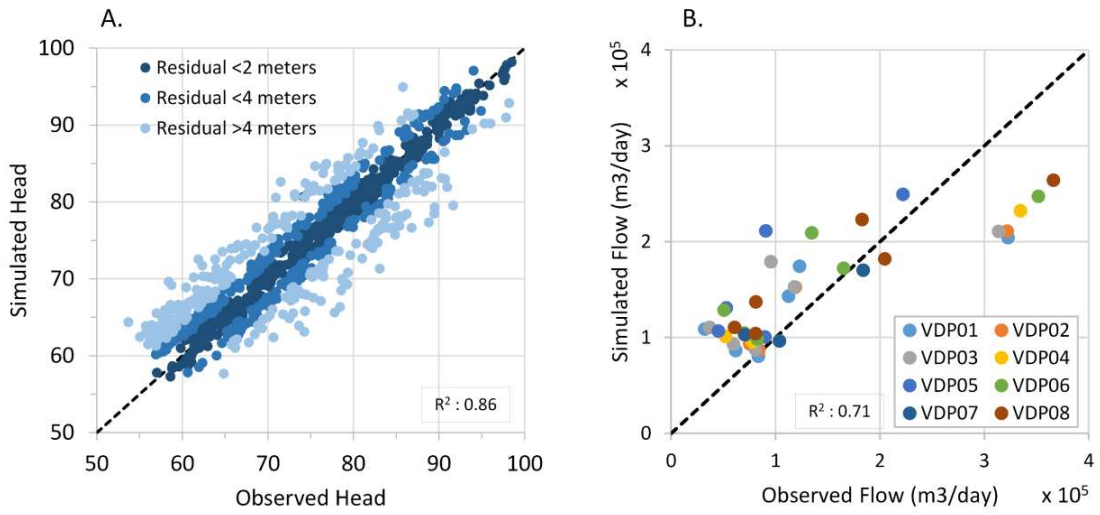

***Figure 5.15**. Simulated vs. calibrated scatter plot for A. observed heads and B. observed stream flow*

After the model was calibrated for the head, it was calibrated with DFG data to simulate the RAE accurately. A total of 57 stream reaches have been parameterized with the

hydraulic conductivity of the river bed. The PSO algorithm has been applied to determine the optimal river bed conductivities to fit the observed DFG data with the methodology discussed in Chapter 3. The calibrated co-relation coefficient of 0.71 (R^2) has been achieved (**Figure 5.15**). The fitted hydraulic conductivity of the river bed has shown a variation from 4.59 $*10^{-4}$m/day to 3.37 $*10^{-3}$ m/day with a mean of 1.76 $*10^{-3}$ m/day.

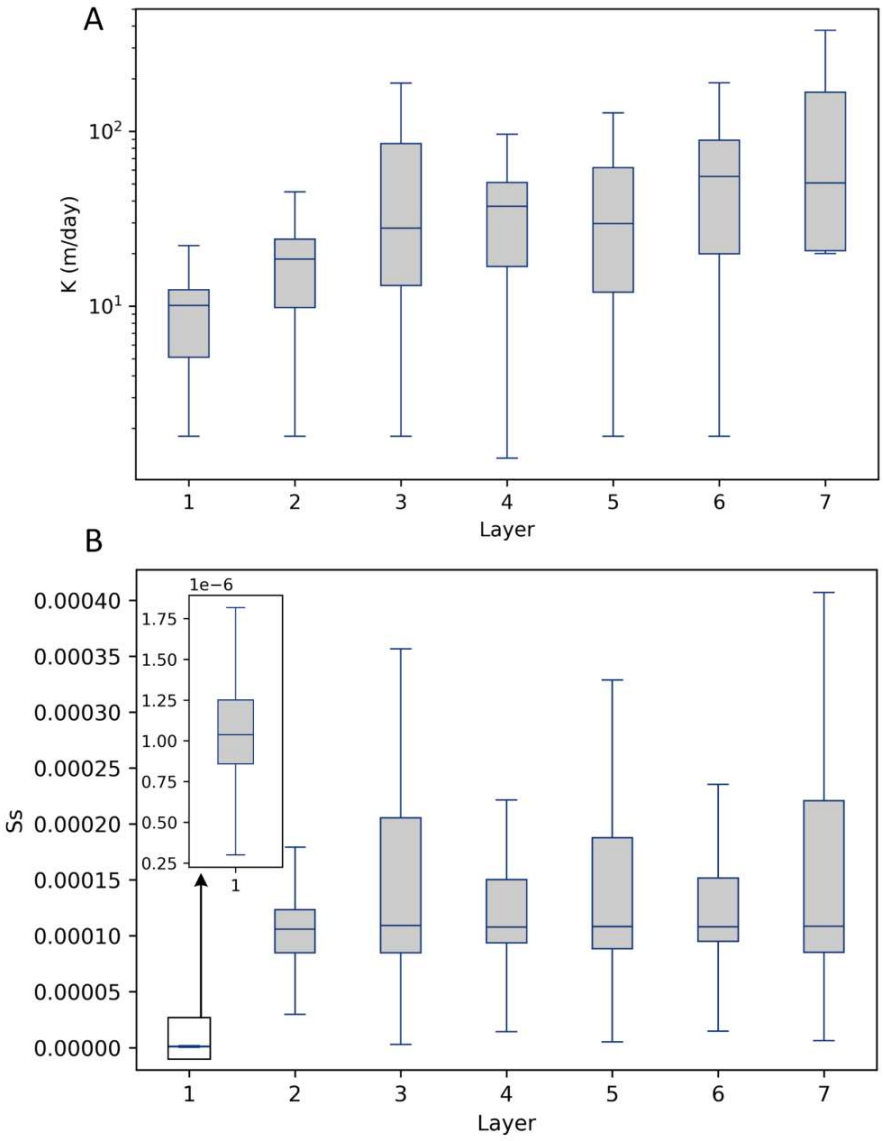

***Figure 5.16**. A. Boxplot of calibrated Hk values and B. Boxplot of calibrated Ss values*

5.8 FORECASTING SW-GW MODEL OF VRB

The forecasting model of VRB has been prepared per four IPCC scenarios (SSP126, SSP245, SSP370, and SSP585) to assess the future water budget and RAE flux amid climate change. The bias-corrected weather parameter data has been used to simulate the SW fluxes in VRB with the calibrated SWAT model of VRB, which has been integrated further into the calibrated GW model to simulate GW fluxes. The detailed forecasting of ancillary data has been explained below.

1. **Inlet Discharge**: Apart from the weather forecast data, the SWAT model of LMGB also required the inlet discharges at the draining watershed outlets. This has been satisfied by forecasting the inlet discharge data using the existing discharge time series data with the LSTM Model. The IPCC scenarios have been taken as independent datasets to map the forecasting to the four scenarios. The LSTM model's hyperparameters have been tuned with Bayesian tuning. The accuracy statistics are presented in **Table 5.5**.

Table 5.5. The LSTM hyperparameter range for inlet discharge prediction

Stations	R2	RMSE	units	dropout	learning_rate	batch_size	epochs
Prayagraj	0.61 – 0.84	440.2-949.8	31 - 46	0.46 – 0.49	0.006 – 0.0065	33 - 65	31 -75
Jaunpur	0.51 – 0.76	23.2 - 47.4	76 - 98	0.5 -0.6	0.01 – 0.02	36 - 58	28 - 56
Meja road	0.62 – 0.78	58.6-103.3	50 - 56	0.5 – 0.58	0.01 – 0.02	18 - 26	67 -81
Pratapgarh	0.58 – 0.86	18.3 – 56.8	82 - 91	0.2 – 0.3	0.005 – 0.0054	38 - 46	28 -48

2. **River Stage**: The forecasted river stage for the RIV package in MODFLOW-NWT has been determined by the simulated discharge from the forecasting SWAT model and the stage-discharge relationship established with an RFR model. The default RFR model has been used as the accuracy was found satisfactory. This is due to the high correlation of river discharge and stage. To check the robustness

of RFR predictions, a 5-fold cross-validation has been performed. The accuracy of the tested dataset has been presented in **Table 5.6**.

Table 5.6. Accuracy statistics of RFR model used for stage determination (*cv-score*: - Cross-validation R2, *cv_std*: - Cross-validation standard deviation)

RIV Nodes	***cv_score***	***cv_std***	R^2
Allahabad	0.98	0.004	0.97
Mirzapur	0.99	0.001	0.99
Mezaroad	0.90	0.011	0.88
Pratapgarh	0.87	0.015	0.85
Varanasi	0.99	0.001	0.99
Maighat	0.65	0.074	0.66
Chunar	0.99	0.002	0.99
Narayanpur	1.00	0.001	0.99
Saidpur	0.94	0.011	0.94

3. **SFR2 Inputs**: All the forecasted input variables for the SFR2 package have been simulated with the forecasting SWAT model for all the scenarios.
4. **Well Demand**: The water demand in the area has been forecasted based on the logistic model. The logistic model of population forecasting is a mathematical technique designed to estimate future population sizes. It uniquely incorporates the concept of carrying capacity, the maximum number of individuals an environment can sustain over the long term without degrading. This model hinges on the logistic growth equation, a formula that captures how population growth accelerates and decelerates in response to available resources and space, ultimately stabilizing as it nears the carrying capacity. The logistic model is expressed as (Delmas, 2004):

$$P(t) = \frac{K}{1 + \left[\frac{K - P_0}{P_0}\right] e^{-rt}} \qquad 5.3$$

Where $P(t)$ is the population at time t, K is the carrying capacity, P_0 is the initial population, and r is the growth rate. The carrying capacity is the maximum

population size of a biological species that an environment can sustain, given the availability of resources such as food, habitat, water, etc (Delmas, 2004). Gretchen C. Daily and Paul R. Ehrlich estimates that India's carrying capacity is around 2 billion people (Daily and Ehrlich, 2016). The average growth rate of Uttar Pradesh from 2001 to 2011 was 2.02% per year. Based on these data, the population demand has been forecasted, assuming that agricultural activity will require more or less the same amount of water while domestic demand will increase logistically. The demand is reaching maximum around mid-century, and the growth rate will decrease after reaching the carrying capacity.

The forecasted data is then used as input for the calibrated GW model to simulate future GW and RAE fluxes in the VRB.

5.9 RESULTS AND DISCUSSION

5.9.1 Future Weather Anomalies in VRB

5.9.1.1 Precipitation

After bias correction, the best climate variable data has been taken to model the basin hydrology. The data from best-performing GCMs has been aggregated by taking the daily mean across all GCMs **Table 5.2**. This data was then further analyzed to assess the climate anomalies and used with the SWAT model to simulate the VRB's hydrology in future scenarios. The four SSPs have been selected, representing pathways corresponding to varying levels of greenhouse gas emissions.

Figure 5.17 presents the forecasted precipitation differences for various Shared Socioeconomic Pathways (SSP) scenarios—SSP126, SSP245, SSP370, and SSP585—each reflecting a range of greenhouse gas (GHG) emission levels. For each scenario, the diagram includes a graph at the top showing the average change in annual precipitation

(measured in millimeters) and, at the bottom, a heatmap that illustrates the variations in precipitation across different locations and time periods.

In **Figure 5.17**.A (SSP126 - low-emissions scenario), the precipitation anomalies vary between positive and negative values, with most years showing relatively moderate deviations from the normal. There are noticeable positive anomalies around 2040 and 2080, reaching up to 20-30 mm, while negative anomalies are more frequent but mild, typically ranging between -20 and -30 mm. The heatmap shows local instances of more extreme precipitation variations, but overall, the anomalies remain moderate, reflecting the relatively stable precipitation patterns expected under low-emission scenarios.

Under the SSP245 (intermediate-emissions scenario) (**Figure 5.17**.B), negative anomalies start to dominate after 2050. Significant drops in precipitation are observed, with values reaching as low as -50 mm in some years (e.g., 2053 and 2089). There are occasional positive anomalies, particularly before 2050, where increases of up to 30 mm are seen. The heatmap highlights more pronounced regional variability compared to SSP126, with certain locations experiencing both extreme wet and dry conditions, particularly in the latter half of the century. For instance, around 2080, several regions show intense negative anomalies, indicating growing disparities in precipitation distribution.

In **Figure 5.17**.C (SSP370 - high-emissions scenario), negative anomalies dominate nearly every year after 2025. Significant reductions in precipitation are evident, with some years (e.g., 2064 and 2095) experiencing anomalies of -75 mm or more. The heatmap shows a widespread and persistent drying trend across most regions, particularly after 2050, with some areas showing extremely dry conditions with anomalies exceeding

-100 mm. The drying trend intensifies post-2050, indicating a marked increase in drought frequency and severity under this high-emissions scenario.

The SSP585 (very high-emissions scenario) (**Figure 5.17**.D) shows even more extreme precipitation patterns. Negative anomalies are widespread, particularly after 2050, with years like 2077 and 2090 showing drops exceeding -100 mm. A few years, such as 2030 and 2070, show positive anomalies, reaching as high as 50-100 mm, but these are rare and localized. The heatmap further reinforces the severity of the drying trend, with many regions showing significant negative anomalies for extended periods. This scenario indicates the most severe and widespread reductions in precipitation, with several regions facing extreme water scarcity.

Understanding the link between specific years and these anomalies is key to grasping how GHG emissions might affect future rainfall patterns. SSP126 demonstrates a balance of positive and negative anomalies throughout the century, with significant increases noted around 2040 and 2080. In contrast, SSP245 identifies a critical shift around 2050, leading to more frequent and intense negative anomalies thereafter. For SSP370 and SSP585, the years after 2050 are of particular interest as negative anomalies become the norm, signaling extended periods of drought. Noteworthy years such as 2064, 2077, and 2090 experienced particularly drastic drops in precipitation, ranging from -75 mm to -100 mm, highlighting the urgent need for water management and ecosystem sustainability strategies in the face of high-emission scenarios.

These findings point to significant adverse effects on surface and GW hydrology, with higher GHG emissions predicting more intense and lasting droughts that affect water sources like rivers, lakes, and reservoirs. This could diminish streamflow, disrupt water supply for various uses, and hinder GW recharge, especially in over-extracted regions.

The spatial variability in precipitation patterns also hints at acute water shortages in specific areas, increasing stress on water resources. Altogether, these changes threaten to destabilize the region's hydrological balance, risking frequent water crises, reduced agricultural productivity, and deteriorating ecosystem health.

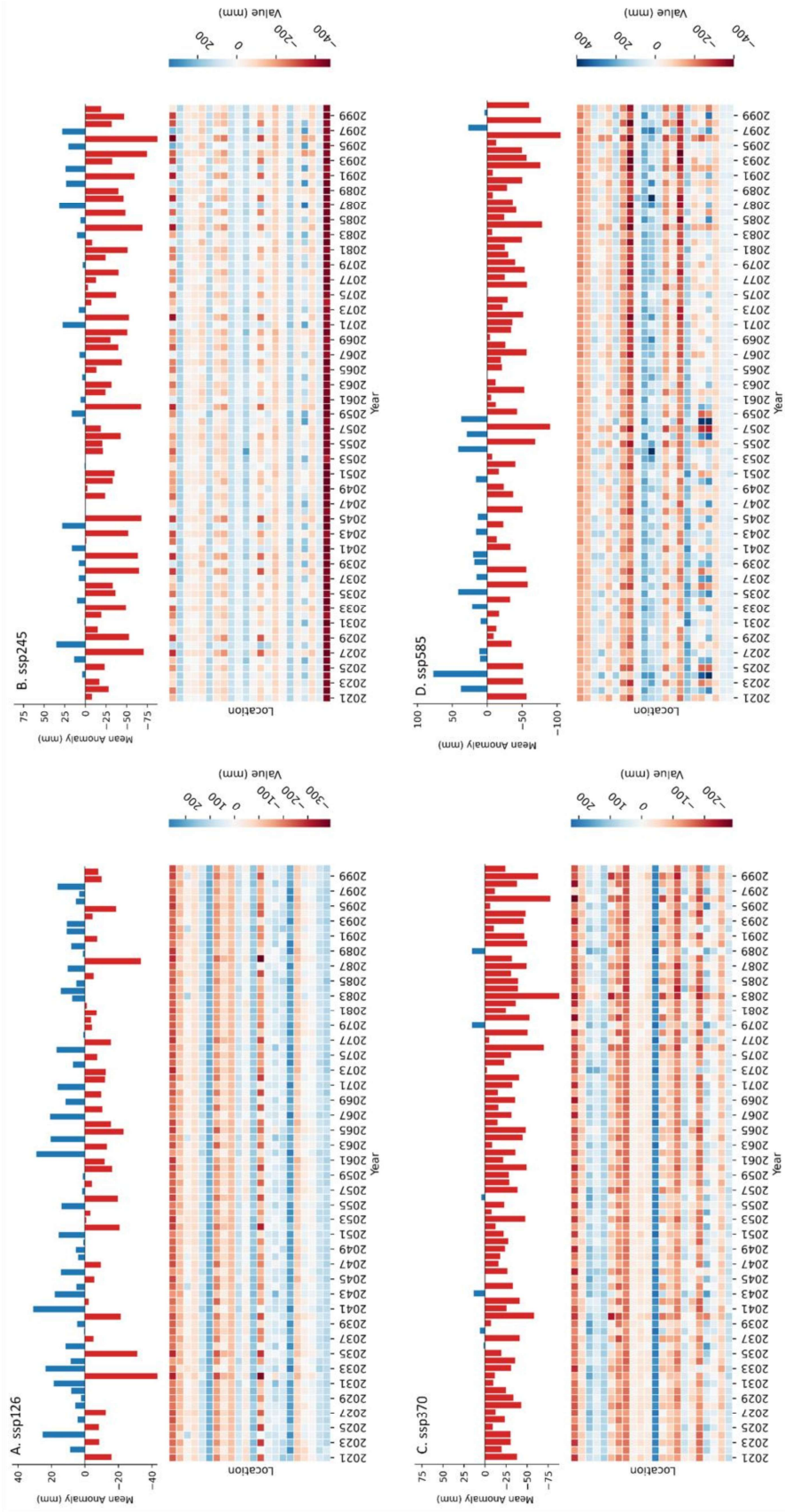

Figure 5.17. *Precipitation anomalies under IPCC scenarios (Each plot highlights the mean annual precipitation anomaly (in millimeters) at the top and a heatmap representing the spatial distribution of anomalies across different locations and years at the bottom)*

5.9.1.2 Maximum Temperature

Figure 5.18 Presents the projected maximum temperature anomalies. In **Figure 5.18**.A (SSP126), the projected temperature anomalies remain largely negative, with most of the years up to 2099 showing negative values. The temperature anomaly fluctuates around -0.2°C to -0.4°C, with a few years showing slightly positive anomalies, especially towards the end of the century, where temperatures reach around 0.2°C above the baseline. The spatial heatmap for this scenario predominantly shows cooler-than-average conditions throughout the 21st century. There are a few isolated instances of minor positive anomalies, but overall, this scenario suggests a relatively stable or slightly cooling trend.

In **Figure 5.18**.B (SSP245), negative temperature anomalies continue to dominate the early part of the century, with values averaging around -0.2°C to -0.4°C. Starting around 2050, there is a noticeable increase in temperature, with anomalies reaching as high as 0.6°C by the end of the century. The spatial heatmap reflects this trend, showing predominantly cool conditions in earlier years and a gradual transition to warmer conditions, especially after 2050. There is significant variability across regions, with some areas experiencing greater warming than others, indicating a growing disparity in temperature changes.

The SSP370 (**Figure 5.18**.C) reveals a stark transition from cooling to significant warming. At around 2040, temperature anomalies are generally negative, averaging around -0.2°C to -0.5°C. Starting from 2040, there is a significant shift in temperature anomalies, with some years showing temperature increases of up to 1.5°C by the end of the century. The spatial heatmap clearly illustrates this change, with most places having cooler-than-average conditions at first, followed by a rapid increase in temperature

anomalies after 2050. By 2099, the heatmap is indicating widespread and severe warming, with many regions experiencing anomalies above 1°C.

In **Figure 5.18**.D (SSP585), the warming trend is the most extreme of all scenarios. In the early part of the century, there is some cooling, with temperature anomalies around -0.5°C. However, there is a quick shift to positive anomalies. After around 2050, the temperature anomalies steadily increase, reaching over 2.0°C by 2099. The spatial heatmap shows a dramatic warming trend, with red shades covering almost all regions by the end of the century. Many areas experience anomalies of more than 2°C, indicating a significant rise in maximum temperatures.

The expected temperature anomalies, specifically in the high-emissions scenarios (SSP370 and SSP585), are likely to have significant negative impacts on the surface and GW hydrology of the study area. With rising temperatures, evapotranspiration rates are projected to increase, leading to a reduction in available water for surface runoff and GW replenishment. The combination of higher temperatures and reduced precipitation, as shown in previous analyses, could worsen drought conditions, leading to a depletion of both SW bodies and aquifers. Additionally, the spatial differences in temperature anomalies suggest that certain areas may be more severely affected than others, potentially resulting in localized water shortages, heightened competition for water resources, and an increased risk of heat-induced stress on ecosystems and agriculture.

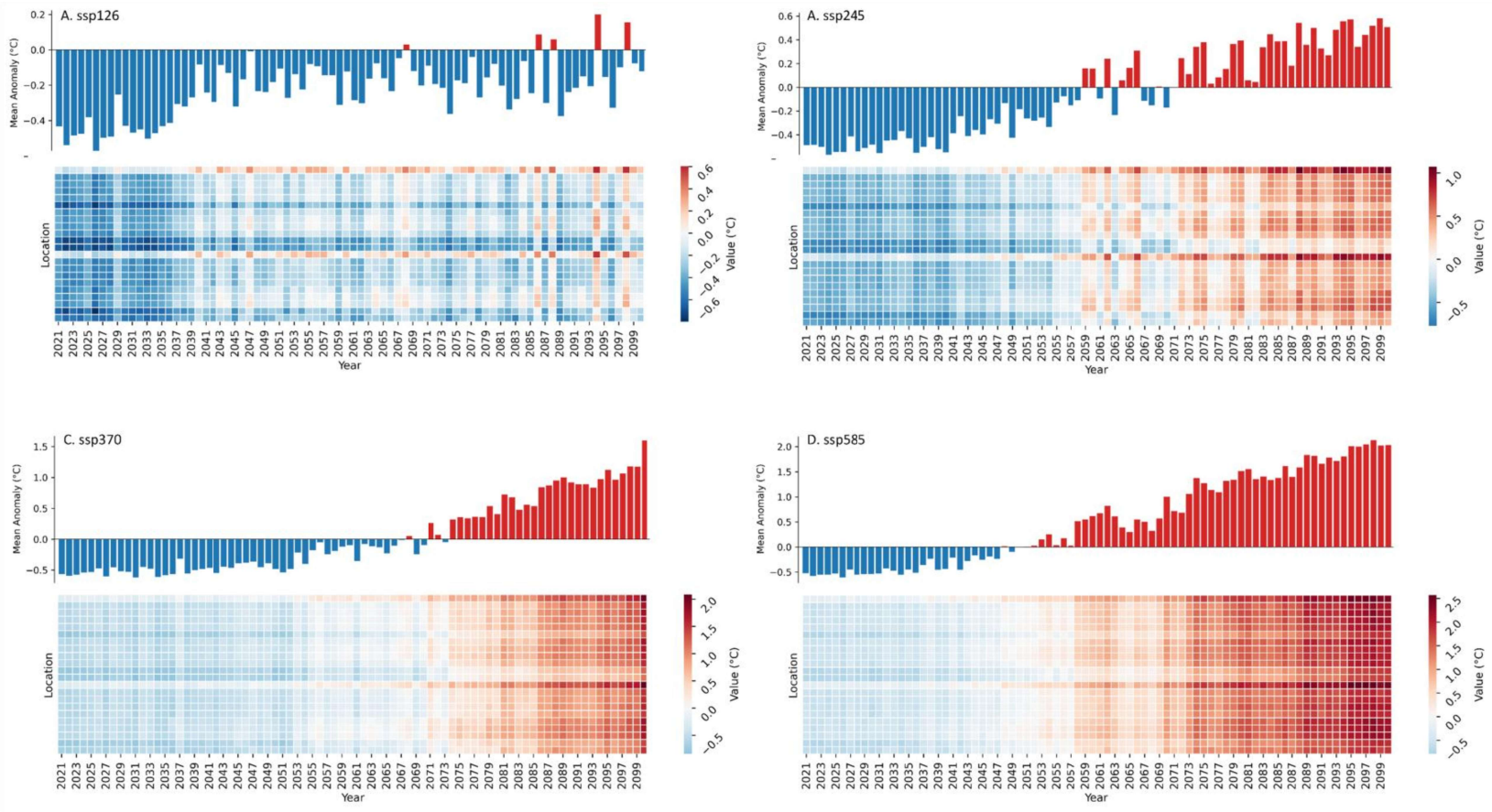

Figure 5.18*.Mean maximum temperature anomalies under IPCC scenarios (Each plot highlights the mean annual maximum temperature anomaly (in C) at the top and a heatmap representing the spatial distribution of anomalies across different locations and years at the bottom)*

5.9.1.3 Minimum Temperature

The mean minimum temperature anomalies consistently show negative values throughout the century for SSP126 (**Figure 5.19**.A). The anomalies range between -0.5°C to -1.5°C, with the lowest values occurring mid-century. The heatmap highlights widespread cooling across most locations. The consistent negative anomalies indicate a prolonged period of cooler-than-average minimum temperatures across the study area, suggesting milder temperatures.

The SSP245 shows mainly negative minimum temperature anomalies ranging from -0.5°C to -1.5°C throughout the century (**Figure 5.19**.B). It indicates slightly stronger cooling, especially in earlier years. Most regions will experience consistent cooling. This suggests that minimum temperatures will remain cooler than baseline values, potentially impacting evapotranspiration rates and GW recharge.

The SSP370 scenario (**Figure 5.19**.C) depicts a major shift in global temperature from cooling to warming, with negative anomalies around -1.5°C in the early part of the century, as shown in prior climate scenarios. However, a dramatic shift occurs around 2080, with temperature anomalies increasing to approximately +1°C by the end of the century, showing a significant warming trend. This scenario also demonstrates increased regional heterogeneity in temperature changes, with some places seeing more pronounced warming than others. The rise in warmer minimum temperatures, particularly after 2080, predicts an increase in nocturnal temperatures, which could worsen heat waves, impair soil moisture retention, and increase evaporation. As a result, these changes may negatively impact hydrological systems, reducing GW recharge and lowering water availability for ecosystems and humans. Overall, the SSP370 scenario highlights the

urgent need for adaptive strategies to mitigate the effects of climate change and enhance resilience in vulnerable regions.

The SSP585 (**Figure 5.19**.D) shows the most extreme warming trend. The anomalies are initially negative, about -1.5°C, but begin to climb rapidly around 2050. By 2099, minimum temperature anomalies will exceed +2°C, showing a substantial warming trend. The heatmap shows that this warming is prevalent throughout the study area, with darker red colors becoming more prominent by the end of the century. This scenario predicts severe warming of minimum temperatures, which might have serious consequences for the hydrological cycle, resulting in increased evapotranspiration, reduced GW recharge, and more frequent and harsh droughts.

The anticipated minimum temperature anomalies under all scenarios point to major effects on the study area's surface and GW hydrology. The sustained dropping of minimum temperatures in the low- and intermediate-emissions scenarios (SSP126 and SSP245) may result in reduced runoff, delayed snowmelt, and decreased GW recharge, all of which would impact the supply of water resources. The late-century transition to significant warming of minimum temperatures in high-emission scenarios (SSP370 and SSP585) may increase evapotranspiration, reduce soil moisture retention, and worsen water scarcity. Rapid warming in SSP370 and SSP585 may also change precipitation patterns, put more stress on water supplies, and increase the frequency and intensity of droughts.

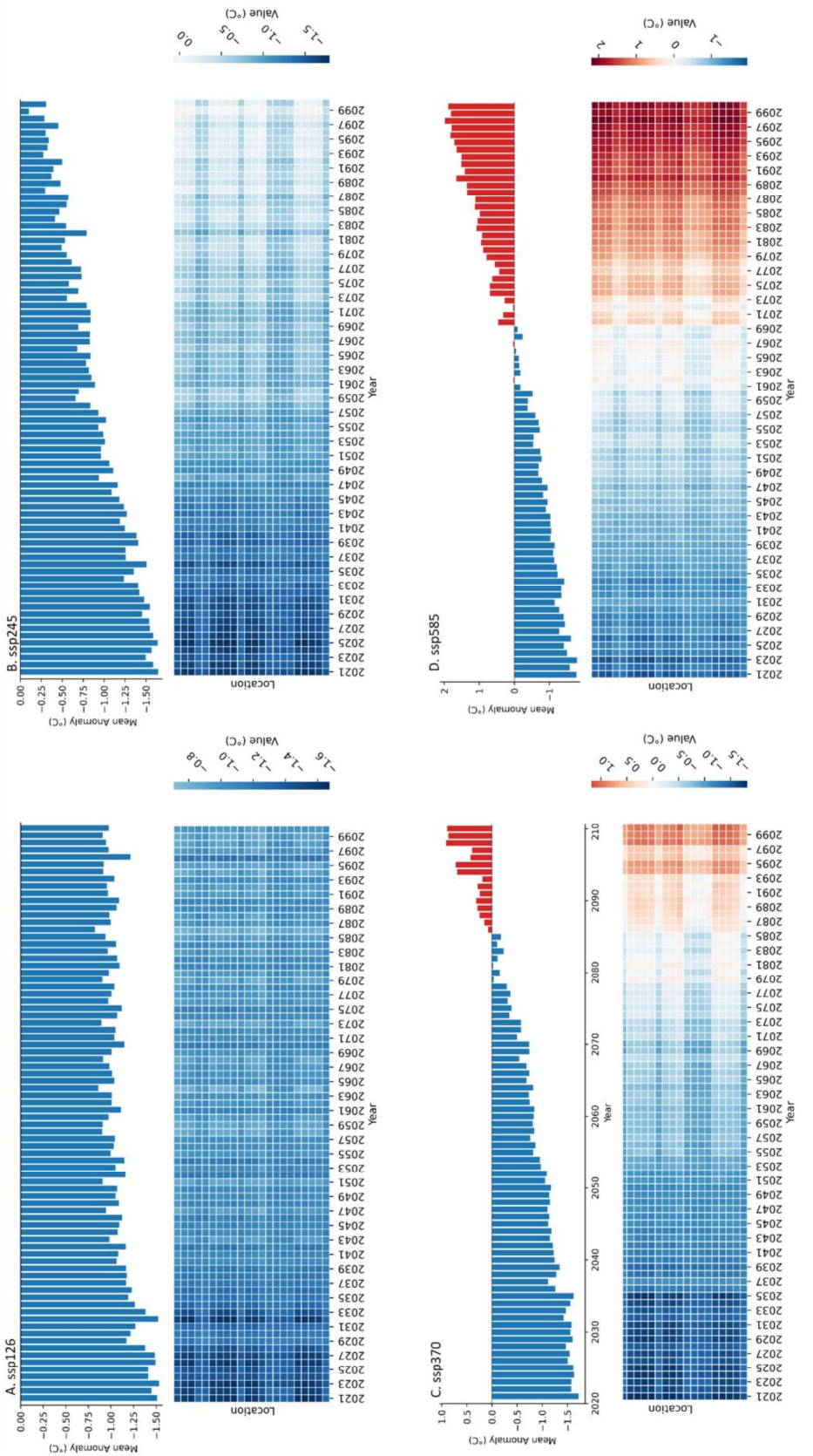

***Figure 5.19**. Mean minimum temperature anomalies under IPCC scenarios (Each plot highlights the mean annual minimum temperature anomaly (in oC) at the top and a heatmap representing the spatial distribution of anomalies across different locations and years at the bottom)Impact of Climate Change on the Natural Recharge*

5.9.2 Natural GW Recharge

GW recharge is a critical hydrological driver to sustain GW storage for agricultural and human use. The extent of GW recharge in an area determines its resiliency towards dry months, and these areas can support streams as a continuous supply of baseflow. Climate change and irrigation expansion are expected to result in more frequent hydrological extremes, such as well drying and flooding. This is particularly worrisome in semi-arid regions, where well drying already causes distress for farmers (Sishodia et al., 2018; Zaveri et al., 2016). Rising temperatures and higher crop water demand have led to increased GW withdrawals and worsening GW depletion rates. This trend is expected to continue and could triple current depletion rates by 2041-2080 (Bhattarai et al., 2023; Dangar et al., 2021; Thampi and Raneesh, 2012). Alterations in land use, combined with urban expansion and fluctuations in climate, have a significant impact on GW levels. A reduction in green spaces and the growth of urban regions are closely linked to the decrease in GW levels observed in fast-developing urban settings (Mall et al., 2006; Mohanavelu et al., 2020). Due to regional variability in the recharge pattern (Thampi and Raneesh, 2012), it is crucial to assess the future GW recharge and identify the recharge hotspots.

5.9.2.1 Trends of Natural Recharge under Climate Change

The future of GW resources looks increasingly uncertain due to the expected impacts of climate extremes. Projections indicate a steady decline in GW recharge rates from 2025 to 2100 across various Shared Socioeconomic Pathways (SSPs), with SSP585 showing the most significant decrease (**Figure 5.20**). This trend highlights the adverse conditions

that could threaten GW sustainability, making it more challenging to meet the needs of both human populations and ecosystems.

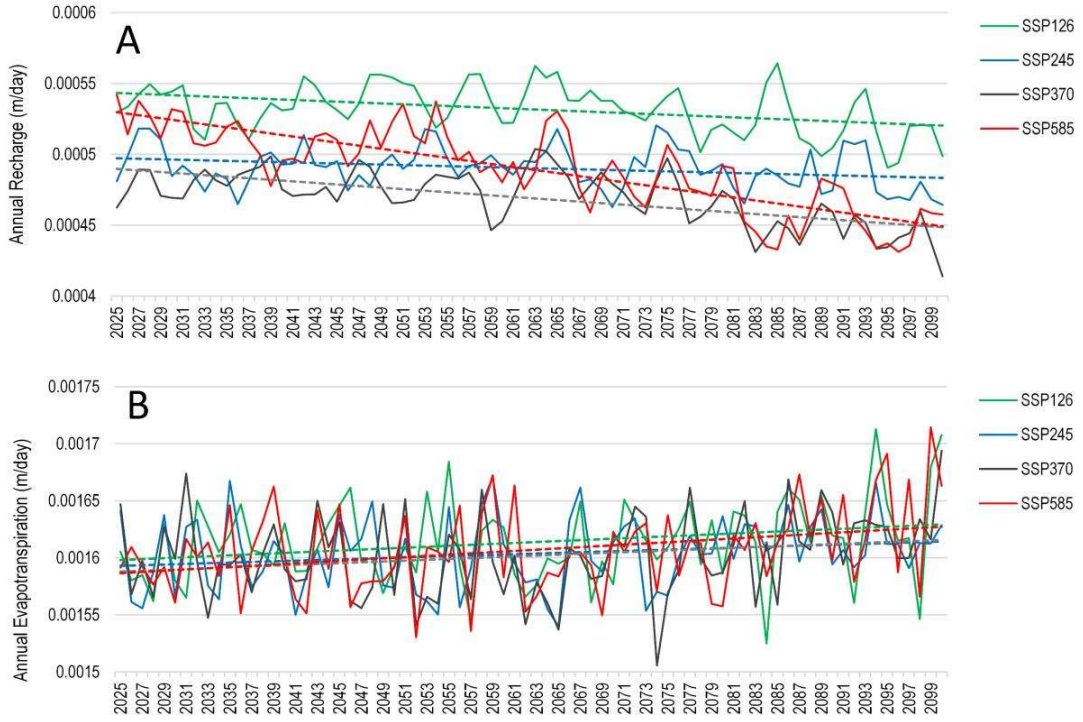

***Figure 5.20**. A. Annual mean recharge rates and trends for all SSPs; B. Annual mean evapotranspiration rates and trends*

While annual evapotranspiration rates remain relatively stable overall, inter-annual variability suggests potential fluctuations that could exacerbate GW depletion during critical periods, especially in regions facing increased evaporative losses. Additionally, the high evapotranspiration rates observed in SSP370 and SSP585 indicate a rising atmospheric demand for water, which may further reduce the capacity for GW recharge. As climatic conditions continue to change—characterized by rising temperatures and altered precipitation patterns—this imbalance may lead to evapotranspiration exceeding recharge, accelerating GW depletion. The implications of this decline are significant, potentially resulting in serious water shortages for agricultural practices, drinking

supplies, and essential ecological systems. Without prompt and effective management strategies, the sustainability of GW resources is at risk, necessitating immediate action to address these challenges for future generations.

5.9.2.2 Recharge hotspots in VRB

Precipitation rates, seasonality in temperature and precipitation, and vegetation and soil structure are important variables in predicting natural GW recharge rates (Moeck et al., 2020). The change in temporal and spatial climatic patterns affects the distribution of recharge areas in a watershed (Gaur et al., 2023). Under climate change, mapping the dynamics of GW recharge and its spatial variability is essential to analyze the resiliency of an area which can be protected. These identified hotspots can be suitable candidates for green zone development to foster natural recharge (Bus and Szelągowska, 2021). The determination of recharge hotspots includes indirect methods such as weighted overlay analysis coupled with multi-criteria decision analysis and machine learning models incorporating the parameters that directly or indirectly affect the GW recharge potential of an area (Lawrence and Upchurch, 1982; Mondal et al., 2012; Rangarajan and Athavale, 2000). The direct methods for recharge zone identification include the hydrological simulation models coupled with detailed soil, land use, and weather data(Gaur et al., 2023) or direct field observations with GW fluctuations and geophysical surveys (Allen, 2009; Chand et al., 2004).

To assess the climate resiliency and recharge hotspots in the VRB, we have employed Anselin's Local Moran's I in ArcGIS to identify clusters of similar recharge values and spatial outliers. The recharge data for the SWAT outputs at the HRU scale has been resampled in the uniform hexagon grids to get better visualizations. The recharge data has been resampled to the decadal mean and further processed in ArcGIS to get the decadal hotspot dynamics.

The results from Anselin's Local Moran's I method reveal distinct spatial patterns of GW recharge under varying climate scenarios, as depicted in the **Figure 5.21**. Under SSP126, the distribution of significant recharge hotspots and coldspots is minimal and relatively stable over time, suggesting a balanced recharge pattern. In contrast, higher-emission scenarios (SSP370 and SSP585) display increasingly extensive and stable clusters of high (hotspots) and low (coldspots) recharge areas, particularly by the mid to late century. This shift indicates a growing disparity in recharge distribution, where certain regions experience intensified recharge while others face substantial declines. The low outliers indicate that the recharge fluxes are more or less similarly distributed, following mainly the rainfall pattern. The influence of soil and land use is minimal due to uniform topsoil-saturated (mainly alluvium) and land-use type (mainly agricultural areas).

The lower part of VRB demonstrated consistent hotspots for increased GW recharge over SSP126, while the middle part of VRB is more dominant in the case of SSP245 and SSP370. In SSP585, the northern part of lower VRB has been a hotspot for GW recharge. A similar pattern has been found for the coldspots, with the lowest disparity in the case of SSP126 and increasing as we go towards SSP585. The upper VRB has shown consistent coldspot region for all scenarios.

In low-emission scenarios like SSP126, the spatial distribution of recharge is relatively balanced (large non-significant areas), supporting long-term GW stability across regions. However, with higher emissions (SSP370 and SSP585), there’s a clear polarization, with intensified hotspots and expanded coldspots. This uneven recharge distribution may lead to GW depletion in some areas and excessive accumulation in others, stressing GW resources and promoting management problems.

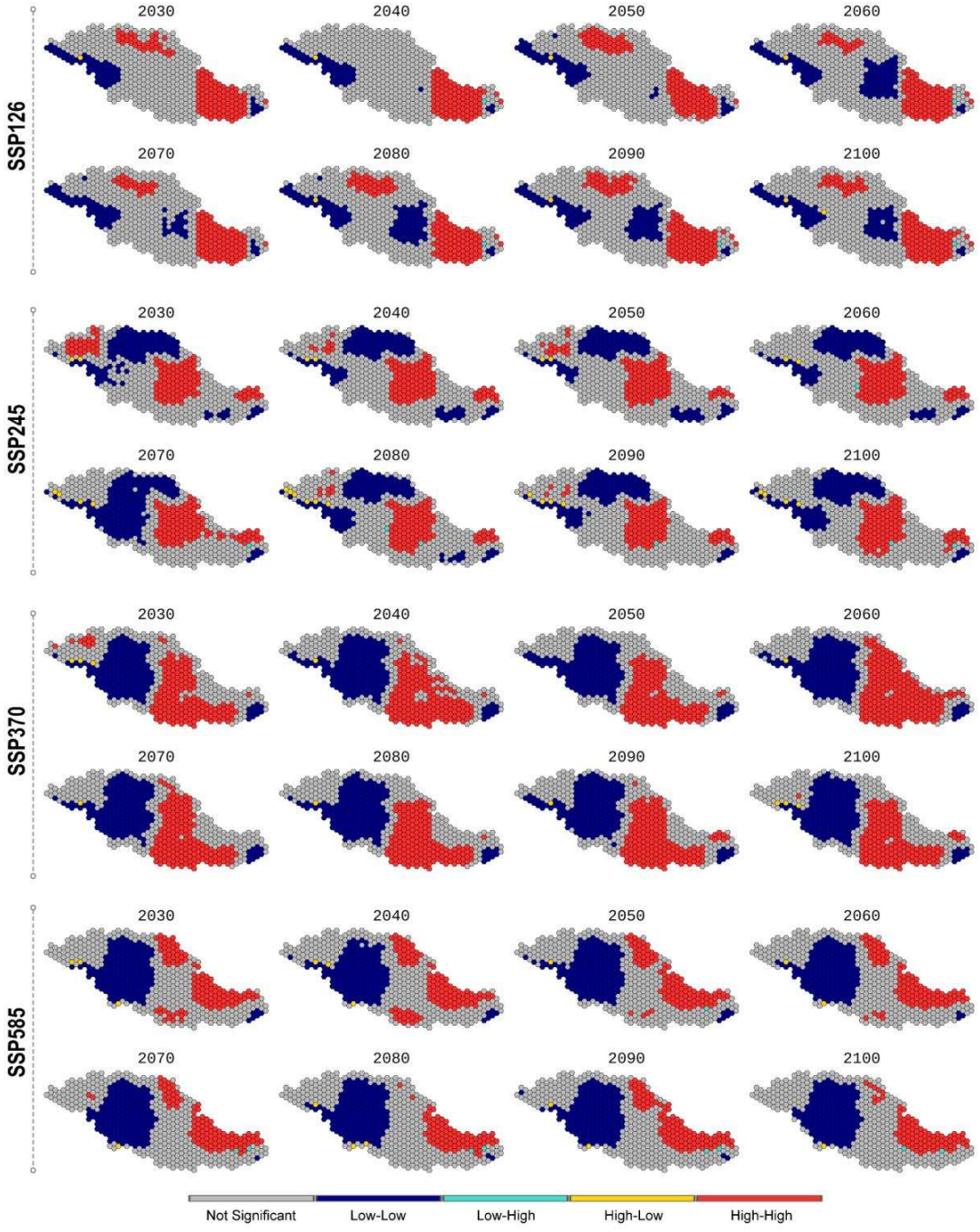

***Figure 5.21**. decadal recharge hotspot dynamics among SSPs*

5.9.3 Dynamics of GW Sustainability Ratio (GSR) in future scenarios

The GW Sustainability Ratio (GSR) is a straightforward tool for evaluating the sustainable use of GW and monitoring its depletion within a specific assessment area.

Assessing the long-term dynamics of GSR is necessary to determine future GW availability. The decadal growth of GSR for IPCC scenarios in VRB has been analyzed using the forecasting SWAT model and forecasted demand. The total net recharge and GW extraction for each decade are then used to calculate the GW Sustainability Ratio (GSR) for all subbasins, as explained in the methodology. The results for each IPCC scenario are presented in *Figures S1* to *S4* in the supplementary material and summarized in **Figure 5.22**.

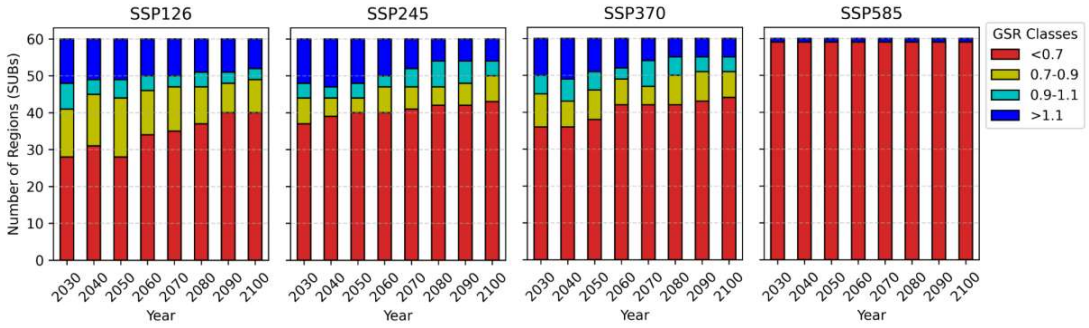

***Figure 5.22**. Stacked bar chart of decadal variation in the GSR classes for IPCC scenarios in VRB*

Figure 5.22 illustrates the decadal variation of the number of subbasins in different GSR classes. The GSR classes represent the areas with sustainable GW extractions, i.e., GSR<0.9 represents the over-exploited areas, and GSR>1.1 represents areas with sustainable GW extraction. GSR between 0.9 and 1.1 represents a more or less balanced condition. Apart from a few subbasins (i.e., GSR >=1), all the subbasins are over-exploited, and the number of subbasins with GSR>1 has shown to decrease as time progresses. The GW demand for most subbasins is quite high, and natural recharge is not enough to cater to these demands, resulting in decreasing GW storage. The low and moderate emission scenarios (SSP126, SSP245) have shown similar conditions, while the number of sustainable areas decreases in high emission scenarios. In SSP585, all the

subbasins have faced over-exploitation, and the net recharge is very low. In many subbasins, it is negative (ET is very high due to high temperature), resulting in low GSR.

The variation in the GW Sustainability Ratio (GSR) across different scenarios is primarily influenced by recharge flux, as the GW demand remains similar in all four scenarios (*The GW demand has been taken similarly and forecasted using the logistic model in all scenarios*). Observing the variability of GSR across the VRB and its temporal fluctuations, it can be safely inferred that GW development in VRB is not sustainable for the future. As the demand for water increases, the gap between available supply and demand widens, indicating that current population growth in Uttar Pradesh is not sustainable. This increase in the GW demand for coming years can deplete the reserved GW storage, altering aquifer properties (Cisneros et al., 2014; Zaveri et al., 2016).

5.9.4 Future SW availability and water demand

The analysis of GSR suggests that natural recharge is insufficient to sustain the VRB's current water demand. To mitigate this difference and support the MAR, identifying a water source for recharge is essential. The surface runoff in excess of the required demand can be stored in the aquifer for later use, as extreme flooding events are imminent in the future. To evaluate the potential use of excess runoff as a future water source, we compared the excess runoff in each subbasin that exceeds the 25% limit with the growing water demand. The runoff generated in excess of the 25% exceedance limit represents the runoff that only exceeds 25% time in a water year, i.e., it only exceeds during monsoon season (Kumar et al., 2024). The flow rates corresponding to 25% exceedance limits are known as 75% dependable flow and have been used widely for water resource management as it is assumed to satisfy all the SW demand (Reddy, 2005). The decadal

variation of GW demand and surplus runoff has been plotted as area plots and provided in *Figures S5* to *S8* in the supplementary material.

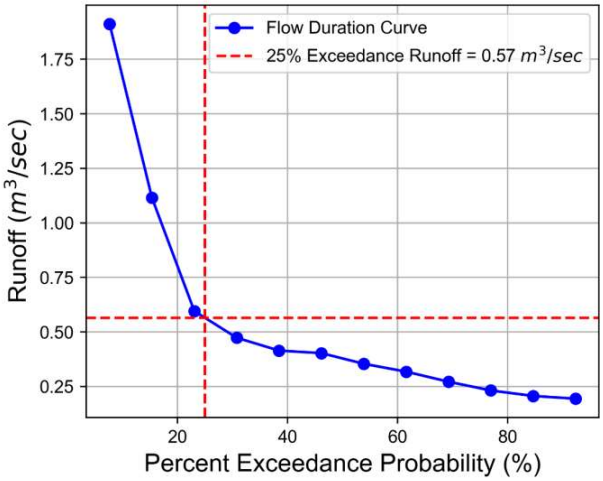

***Figure 5.23**. Example Flow Duration Curve and runoff flux corresponding to 25% exceedance limit*

It is observed that the overall surplus runoff is almost similar in all IPCC scenarios. However, the spatial distribution has shown large variation (*Figures E2 – E5 of the supplementary material*). Even the high-emission scenario (SSP585) has also shown high runoff potential. This is justified by climate change affecting extreme events more than reducing total volume. The increased rainfall intensity reduces GW recharge (Gaur et al., 2023). Managed Aquifer Recharge (MAR) has become essential to mitigate the loss of GW recharge, as around 67% of the population relies on GW for drinking purposes (Dillon, 2005; Dillon et al., 2019; Kumar et al., 2024).

In all scenarios, the surplus runoff volume of approximately 70% of the subbasins is 10-30% of the growing GW demand (*Please refer to supplementary material*). However, approximately 20% of the subbasins have a surplus runoff volume of about 30-70% of GW demand. Four subbasins have very little GW demand compared to the generated excess runoff volume. If injected into the aquifer, this excess runoff volume can help

replenish the natural GW to meet the additional demand for GW (above current natural recharge). The shift in the GSR has been plotted in **Figure 5.24**, after assuming that 100% of the future surplus runoff (above the 25% exceedance limit) in all the SSPs will be recharged through MAR. The results indicate that the incorporation of artificial recharge improves the GSR, shifting approximately 25% of subbasins to the sustainable category (GSR>1) in SSP126 and SSP245 (**Figure 5.24**). The SPP370 shows a shift of approximately 15 % of the subbasins to the sustainable category (GSR>1). The SSP585 has not shown any shift from the previous conditions, which shows that the high-emission pathway can result in an undesired hydrological impact on the VRB.

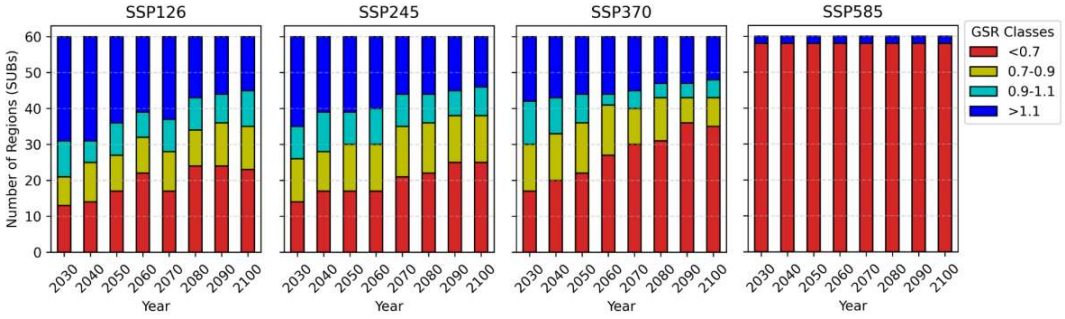

***Figure 5.24**. Stacked bar chart of decadal variation in the GSR classes for IPCC scenarios in VRB with MAR*

5.9.5 Climate Change Impact on the RAE

It is crucial to understand how rivers and aquifers interact in order to effectively manage water resources, especially during dry periods. This is vital for maintaining a consistent flow of water during times of drought, which is important for supporting ecosystems, agriculture, and overall water availability. Excessive withdrawal of GW, particularly during droughts, can significantly reduce the flow of water in rivers. This is especially noticeable in agricultural and urban areas, where heavy extraction of GW leads to lower river flow, impacting aquatic habitats and overall water availability (Karki et al., 2021;

Singh et al., 2017). Apart from this, understanding the response of MAR to RAE is essential to develop an effective system to augment low flows in rivers connected to alluvial GW systems (Ronayne et al., 2017).

To understand the dynamic of RAE in VRB, the integrated SW-GW model has been calibrated with DFG observations. The weather data from IPCC scenarios of CMIP6 models has been used to simulate future RAE variability. The current analysis shows the current and future RAE dynamics in VRB.

5.9.5.1 RAE in VRB

The RAE flux from January 2022 to December 2023 has been plotted as contour maps for the main stretch of the Varuna River and all the tributaries of the Varuna River (Basuhi and Morwa) (Figure 5.25). In these plots, blue regions indicate where the river is losing water to the aquifer (+ve stream leakage), while red regions show where the river is gaining water from the aquifer (-ve stream leakage).

The Varuna River shows significant variability along its length, with alternating zones of river loss (blue) and river gain (red). Near the Ganga River (chainage ~160-200 km), the river experiences substantial water loss to the aquifer, indicated by widespread blue areas, suggesting that the river acts as a recharging source for the aquifer in this region. The river exhibits gaining properties near and around the confluence of Morwa and Basuhi to Varuna. Additionally, an intense gaining reach is visible near the cantonment area (chainage ~215-230 km). Seasonality in the interaction is evident, with peak river loss values during the monsoon season ranging from ~1000 to ~2300 m3/day. Most of the stream reach becomes gaining during the summer, with values ranging from ~200 to ~500 m3/day.

The Morwa River consistently loses water (shown in blue) along most of its path, indicating that it mainly recharges the aquifer. This is especially noticeable in the upstream areas (0-30 km), where the river consistently loses water to the aquifer, leading to lower GW levels. The net contribution of RAE to the stream flow varies from ~2% to ~12%, depending upon wet and dry seasons, respectively.

The Basuhi River (bottom plot) follows a similar pattern, where it predominantly shows negative leakage (blue), indicating it is also a losing river for much of its length. However, there is considerable variability in the leakage pattern, with several areas alternating between gaining and losing water.

5.9.5.2 Forecasted RAE

The monthly forecasted RAE has been plotted as contour plots and provided in Appendix E. Further, the impact of climate change on the decadal variation of mean annual RAE flux has been analyzed and plotted for Varuna, Basuhi, and Morwa from **Figure 5.26** to **Figure 5.28** for all scenarios.

The forecasted RAE flux represents the effect of increased GW extraction in the rivers. The net GW demand has been doubled by the end of 2100 as per the logistic model of the study area. This results in a substantial GW level decline ranging from ~3m to ~8m for the low emission scenario (SSP126) and high emission (SSP585) scenario, respectively. This GW decline has been reflected in the RAE flux, leading to the slow loss of the connection between the river and aquifer in the VRB. For all scenarios, the gaining stream reaches shifts to losing by the end of 2100 (Figure 5.26). The shift for SSP585 is rapid, with an instant transition from gaining to losing evident after 2020 for the gaining reaches.

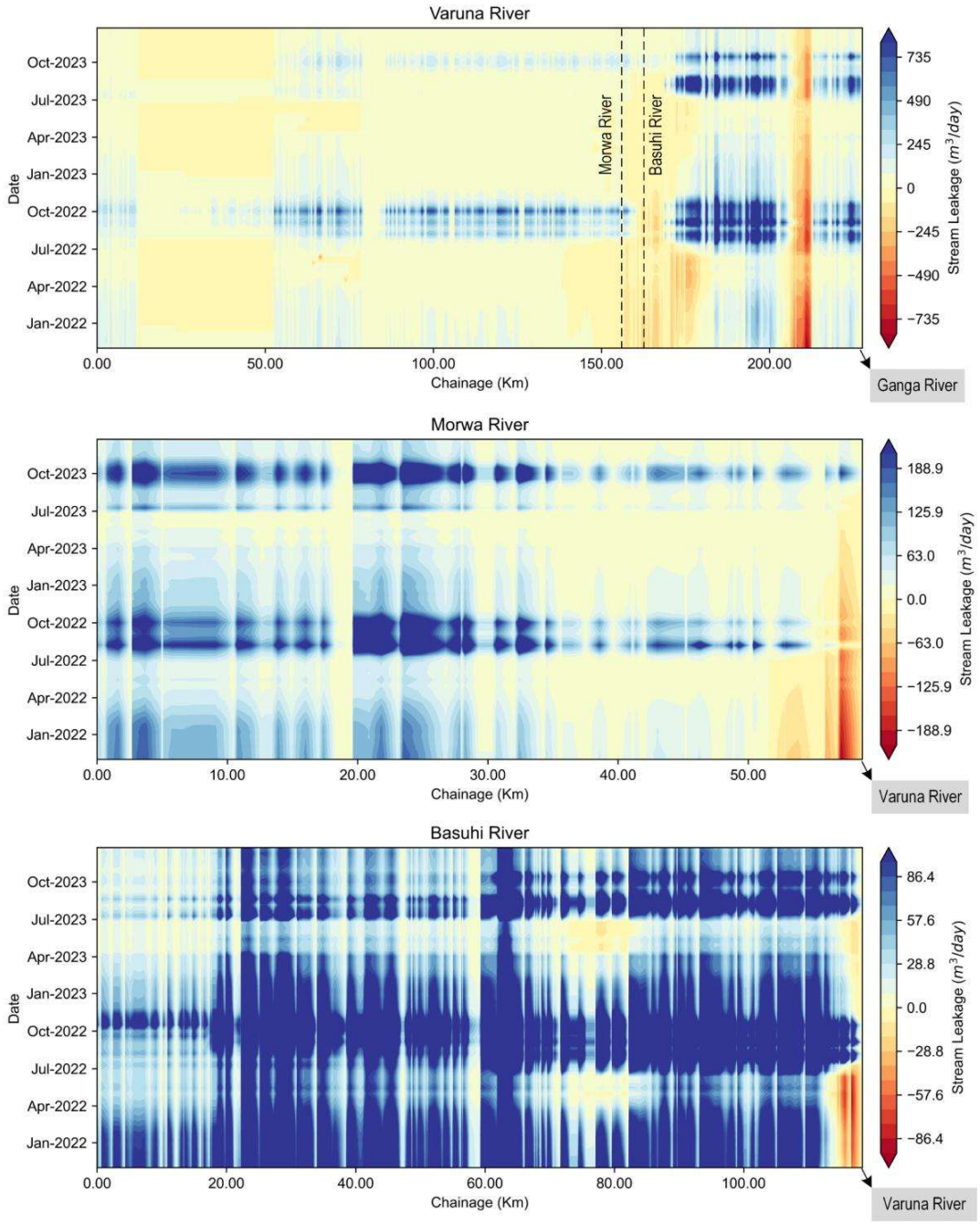

Figure 5.25. *Contour plot of RAE flux in VRB. The chainage has been taken from the lower-order reaches.*

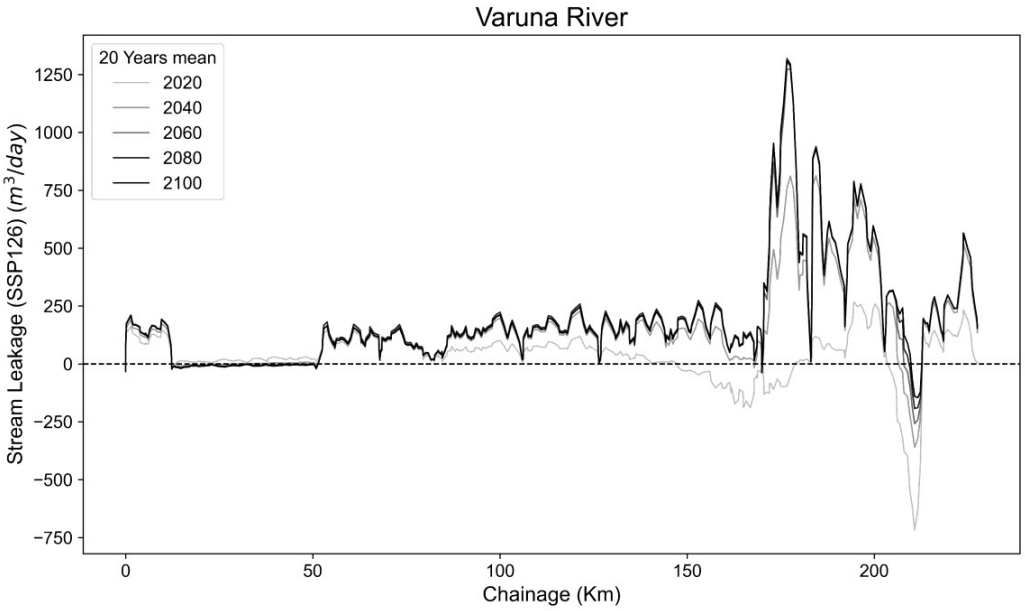

***Figure 5.26**. Variation of annual mean RAE in Varuna River per 20 years for all IPCC scenarios*

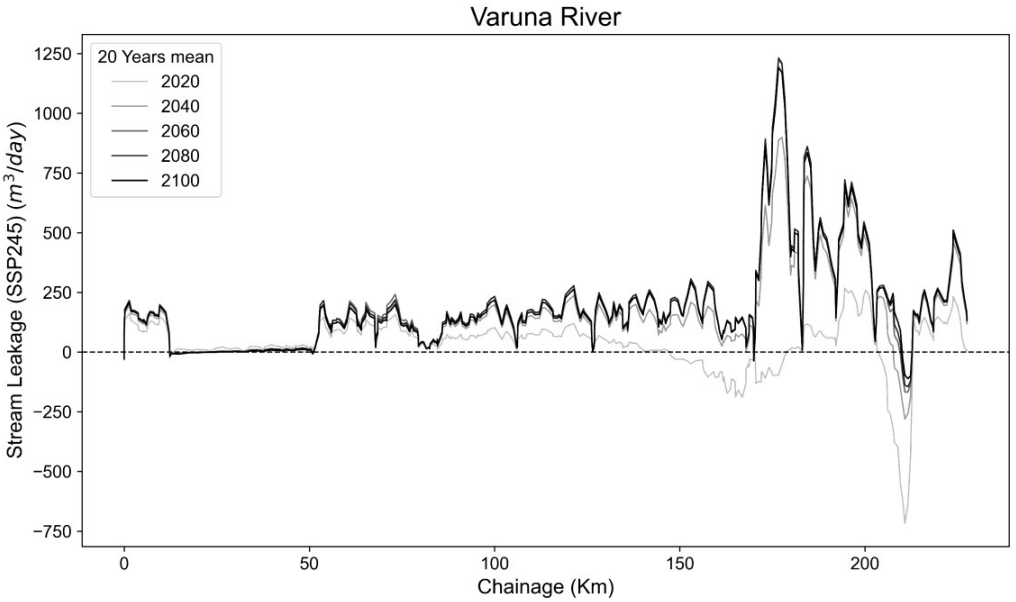

Figure 5.26 (continue…)

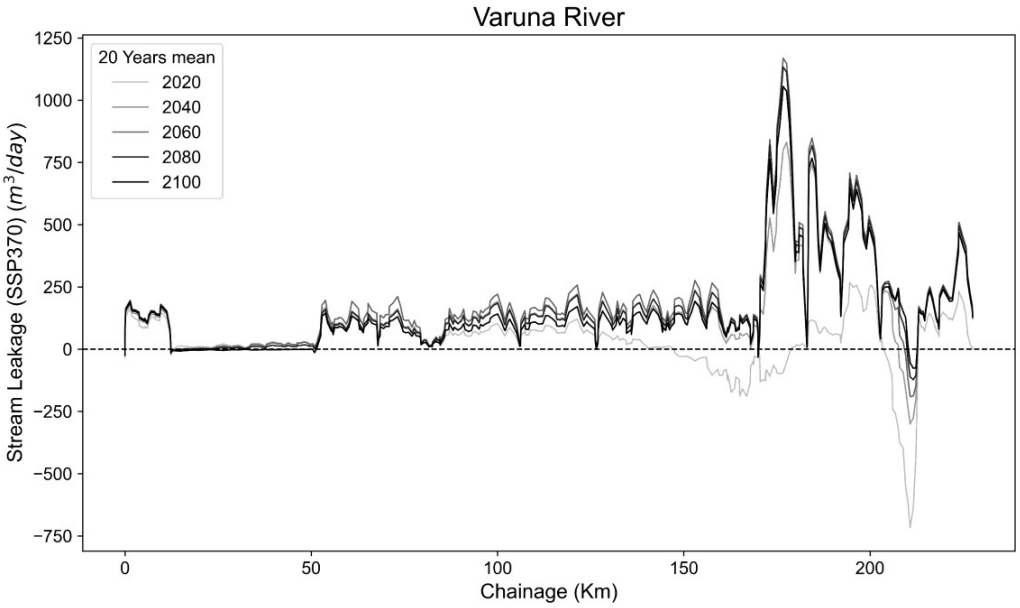

Figure 5.26 (continue…)

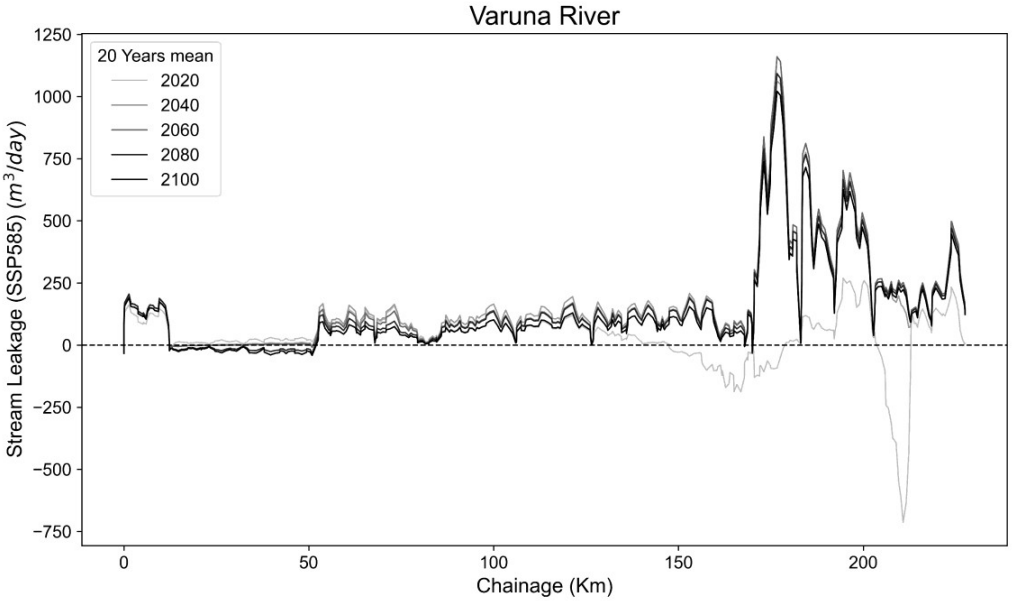

Figure 5.26 (continue…)

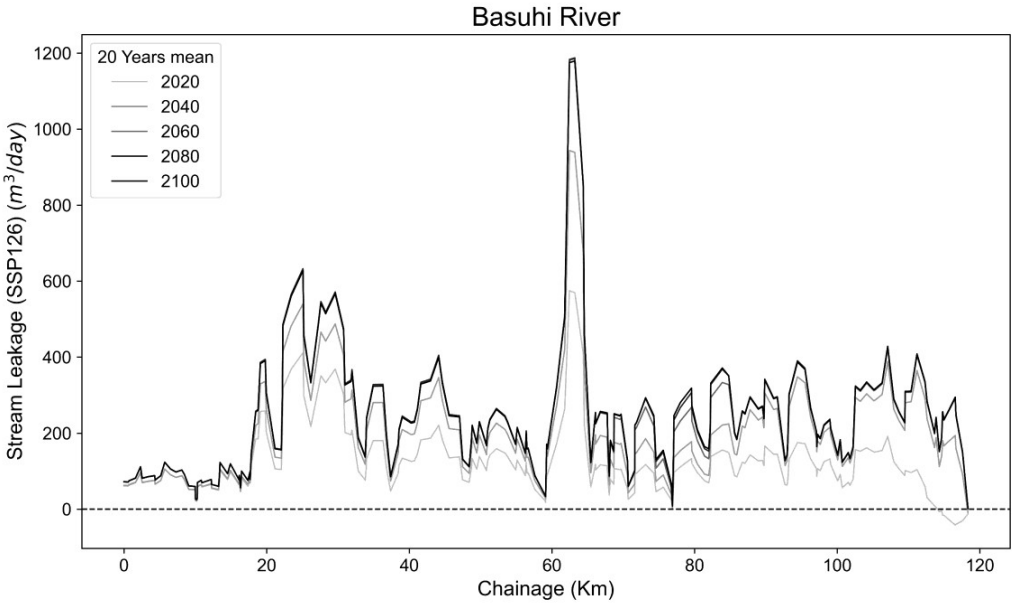

***Figure 5.27**. Variation of annual mean RAE in Basuhi river per 20 years for all IPCC scenarios*

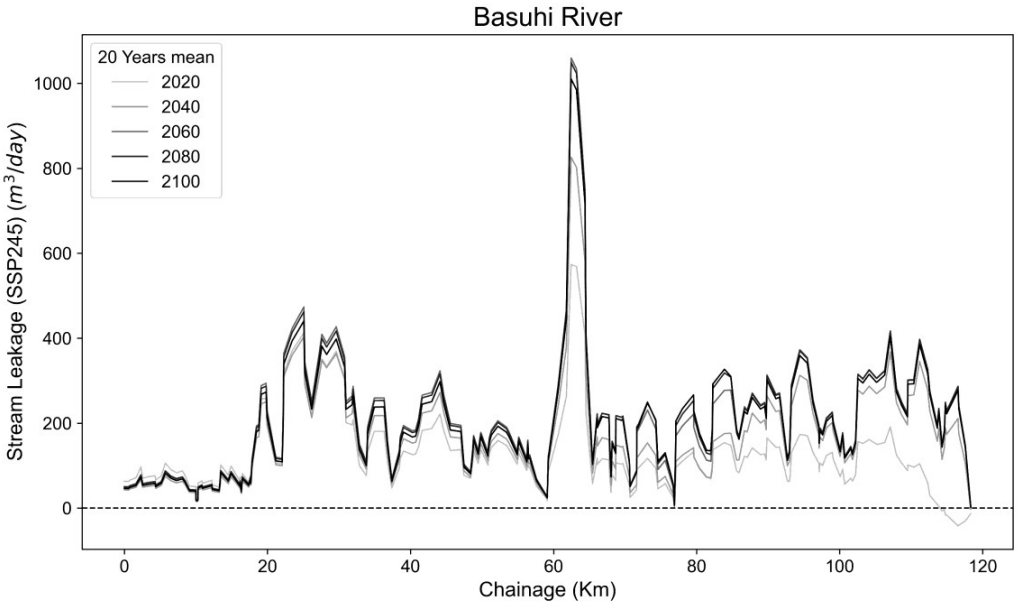

***Figure 5.27** (continue…)*

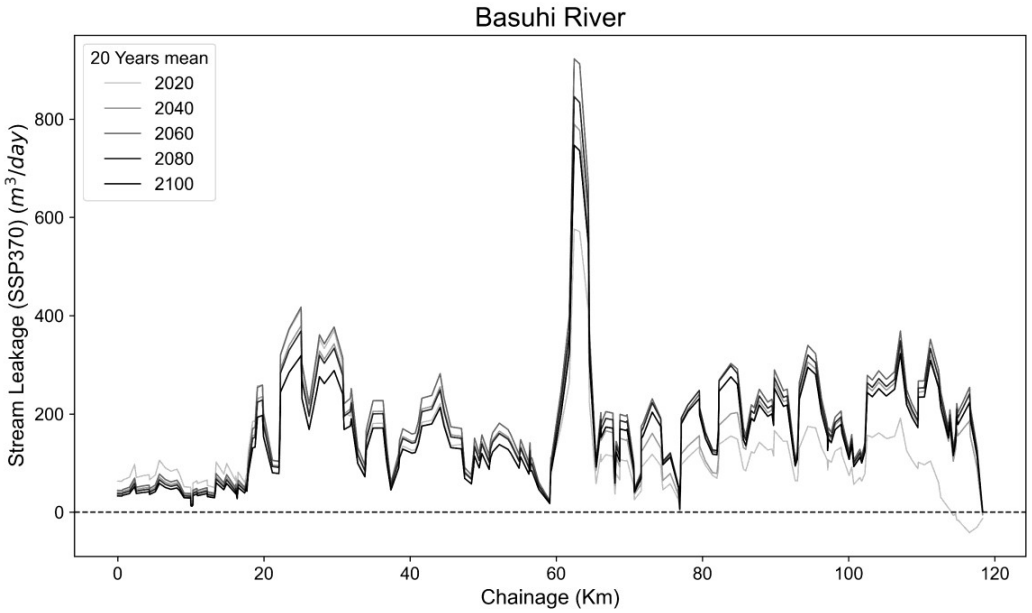

Figure 5.27 *(continue…)*

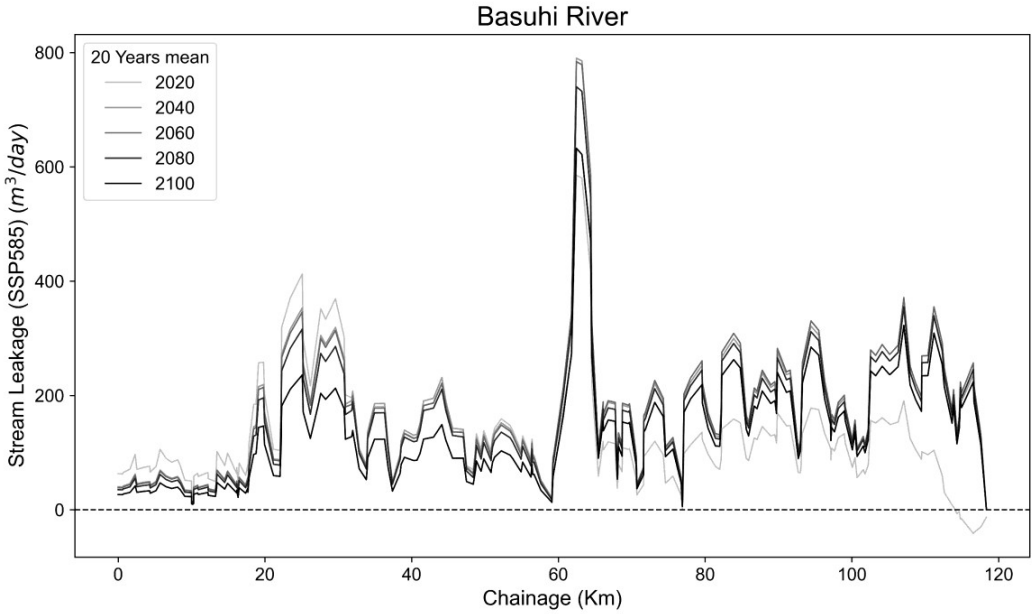

Figure 5.27 *(continue…)*

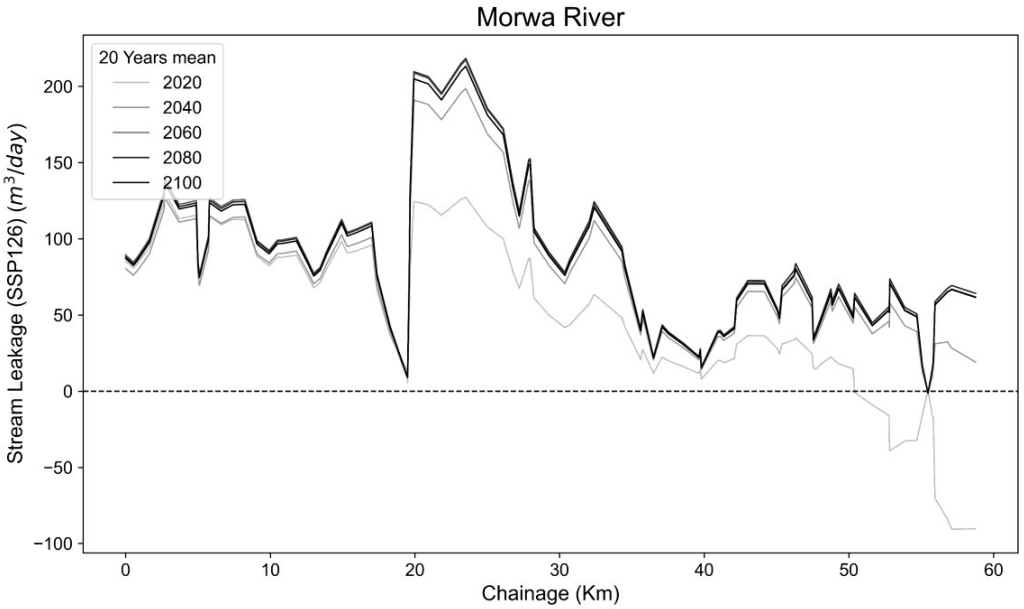

***Figure 5.28**. Variation of annual mean RAE in Morwa river per 20 years for all IPCC scenarios*

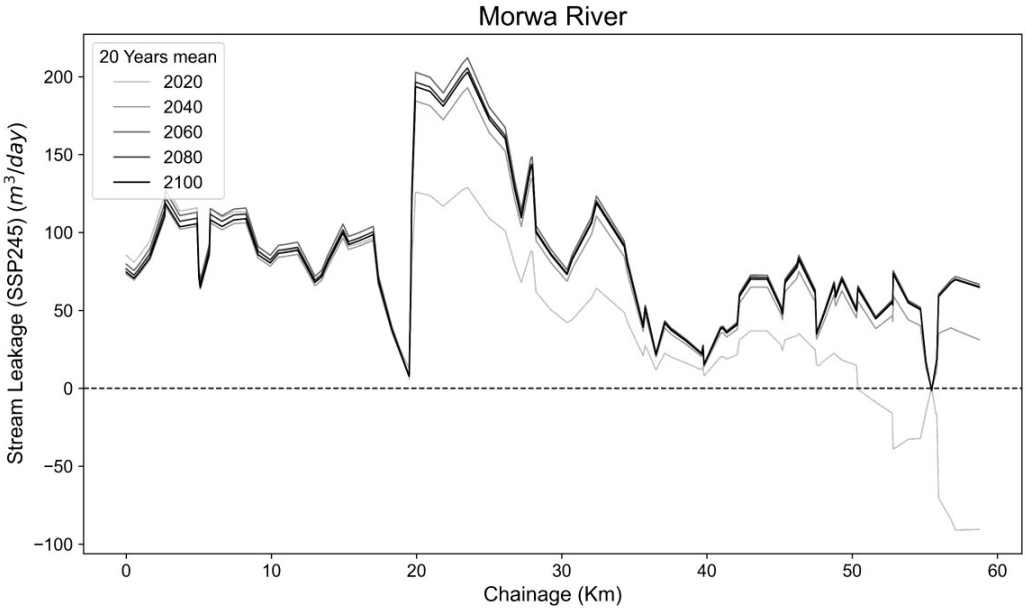

***Figure 5.28** (continue…)*

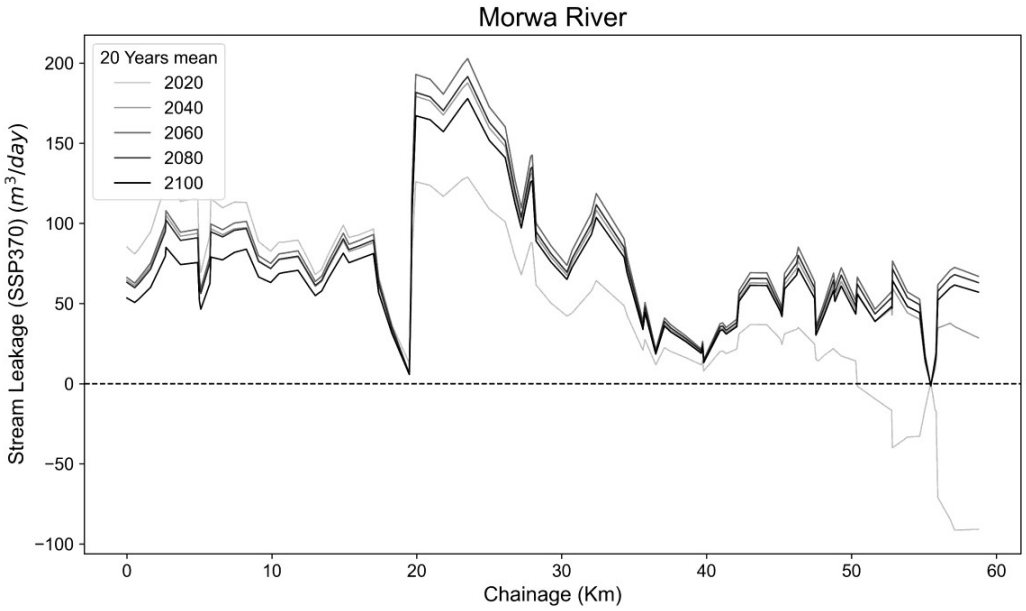

Figure 5.28 *(continue…)*

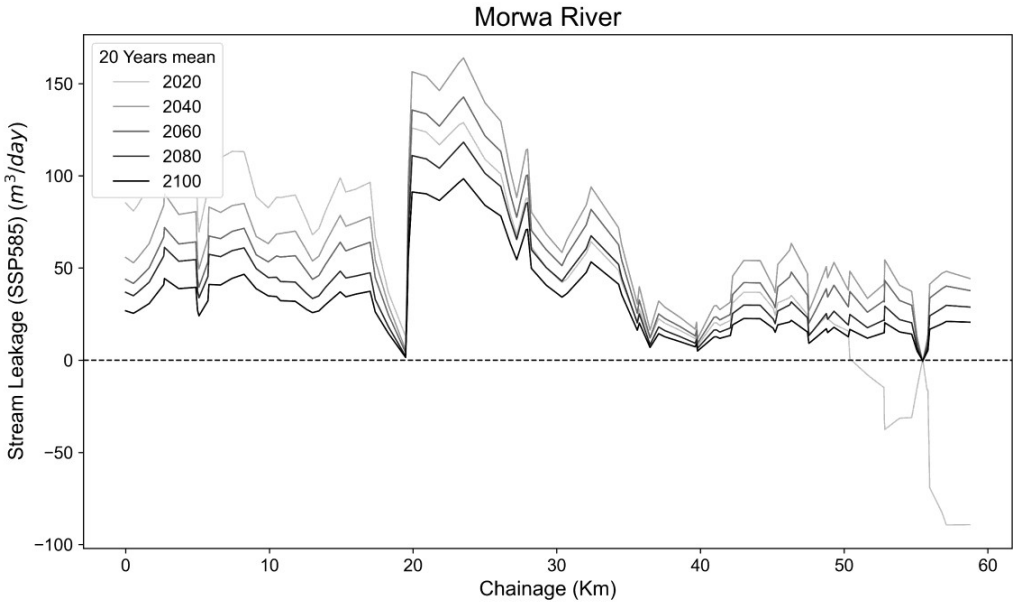

Figure 5.28 *(continue…)*

5.10 SUMMARY

This chapter focuses on the assessment of the Deterministic Climate Change Impact Study on the River-Aquifer Exchange (RAE), utilizing an integrated SW-GW model. The

calibrated Soil and Water Assessment Tool (SWAT) model has been employed to conceptualize the GW system. Subsequently, a loosely coupled model of the Varuna River Basin (VRB) was calibrated for GW heads and RAE using data collected from the Distributed Grid (DG) approach for specific time steps. Outputs from the Coupled Model Intercomparison Project Phase 6 (CMIP6) for four carbon emission pathways have been applied to simulate the forecasting models of the VRB.

Based on the results and discussions in the previous sections, the following broad conclusions have been drawn: The BCC-CSM2-MR, MIROC-ES2L, and MPI-ESM1-2-HR models from CMIP6 demonstrate a better simulation of the Indian monsoon compared to the other models studied in this research when analyzed against the IMD 2D gridded data. Climate change is influencing both the intensity and spatial pattern of rainfall across all scenarios, with a maximum reduction in annual precipitation ranging from -75 mm to -100 mm. Extreme temperature events are also observed to be increasing, with maximum temperature anomalies rising by 2°C and minimum temperatures increasing by 2°C by the end of 2100, compared to the baseline period of 1975-2020.

The sustainability of GW development under climate change has been evaluated using the GW Sustainability Ratio (GSR). Given the variability of GSR across the VRB and its temporal fluctuations, it can be concluded that GW development in the VRB is not sustainable for the future. Natural recharge currently fulfills only 20% to 80% of the total GW demand (GSR: 0.2 – 0.8), with the remainder coming from either GW storage or upstream boundary leakage. This depletion of GW reserves has resulted in a decline of the GW table by 3 to 8 meters across the VRB according to different IPCC scenarios. Such a drop in the water table could adversely affect the interaction between SW and GW in the Varuna River.

The surplus runoff—defined as the runoff volume exceeding the runoff events with a 25% exceedance probability—from subbasins could serve as a crucial resource to meet additional GW demands that are not replenished through natural recharge. For all scenarios, surplus runoff water could contribute between 20% and 80% of the total GW demand in the VRB. This indicates that Managed Aquifer Recharge (MAR) using storm runoff could provide a viable solution to GW depletion in the region.

The RAE in the Varuna River and its tributaries have been assessed. The river exhibits a dynamic interaction with the GW system, showing a losing state during the monsoon season and a gaining state during dry periods (pre-monsoon). The net contribution of RAE to streamflow fluctuates from approximately 2% to 12%, depending on the wet and dry seasons, respectively. RAE has been decreasing due to climate change. The reduction in natural recharge coupled with rising GW demand has resulted in a declining GW table, disrupting the connection between the river and the aquifer. This phenomenon has significantly impacted the baseflow of the Varuna River, as many gaining river sections are projected to diminish after 2050.

In conclusion, the Varuna River is at risk of losing its dry flow as a result of climate change and increasing GW demand. To address the issues of declining GW tables and diminishing RAE, it is essential to plan for Managed Aquifer Recharge (MAR) in the basin, allowing surplus water to be injected into the aquifers during wet months, which have previously led to flooding.

***